Title

Structural Determination of p2Mg(2x1)CO/Ni(110) With The Use of Angle-Resolved Photoemission Extended Fine Structure

Journal

Physical Review B, 48(3)

Authors

Huang, Z.Q.
Hussain, Z.
Huff, W.T.
et al.

Publication Date

1992-08-05

LBL-32713
UC-401
Preprint

Lawrence Berkeley Laboratory
UNIVERSITY OF CALIFORNIA

CHEMICAL SCIENCES DIVISION

Submitted to Physical Review B

Structural Determination of p2mg(2x1)CO/Ni(110) Using Angle-Resolved Photoemission Extended Fine Structure

Z.Q. Huang, Z. Hussain, W.T. Huff, E.J. Moler, and D.A. Shirley

August 1992

Prepared for the U.S. Department of Energy under Contract Number DE-AC03-76SF00098

DISCLAIMER

LBL-32713
UC-401

Structural Determination of p2mg(2x1)CO/Ni(110) Using Angle-Resolved Photoemission Extended Fine Structure

Z.Q. Huang, Z. Hussain, W.T. Huff, E.J. Moler, and D.A. Shirley

Department of Chemistry
University of California

and

Chemical Sciences Division
Lawrence Berkeley Laboratory
University of California
Berkeley, California 94720

August 1992

This work was supported by the Director, Office of Energy Research, Office of Basic Energy Sciences, Chemical Sciences Division, of the U.S. Department of Energy under Contract No. DE-AC03-76SF00098.

Structural Determination of p2mg(2x1)CO/Ni(110) Using Angle-Resolved Photoemission Extended Fine Structure

Z.Q. Huang, Z. Hussain, W.T. Huff, E.J. Moler, and D.A. Shirley

Department of Chemistry, University of California, Berkeley and Chemical Sciences Division, Mail Stop 2-300, Lawrence Berkeley Laboratory, 1 Cyclotron Road, Berkeley, California 94720

The technique of angle-resolved photoemission extended fine structure has been used to study the chemisorption geometry of the dense p2mg(2x1)CO/Ni(110) overlayer at low temperatures. Photoemission intensities from the carbon 1s core level were measured in three directions as functions of photoelectron kinetic energy in the range 60-400 eV. Using multiple-scattering spherical-wave modeling, it was found that the CO molecules are adsorbed on the short-bridge sites, with adjacent CO molecules along the $[1\bar{1}0]$ direction displaced alternatively in opposite directions towards the [001] and the $[00\bar{1}]$ azimuths to form a zigzag chain geometry. The tilt angle is 16±2° from surface normal for the direction linking the carbon atom and the center of the nickel bridge. The carbon-nickel interatomic distance was determined to be 1.94±.02Å. The first to second nickel layer spacing is 1.27±.04Å, up from 1.10Å for the clean Ni(110) surface, but close to the 1.25Å Ni interlayer spacing in the bulk. Using the findings of earlier studies of this system, the C-O bond length and tilt angle were varied within small ranges (1.10-1.20Å and 15-23°, respectively) in our MSSW simulations. At 1.16Å and 19° the best agreement between the experimental data and the theoretical simulations was achieved. The above results yields an O-O distance of 2.95Å for the two nearest CO molecules, close to twice the van der Waals radius (~1.5Å) for oxygen.

I. INTRODUCTION

Dense atomic and molecular overlayers on metal surfaces are of great interest because these systems often exhibit unusual atomic arrangement and surface symmetry.[1-3] While at low adsorption coverages the structures and properties of surface overlayers are generally more influenced by the interaction between the adsorbed molecules and the metal substrate, the adsorbate-adsorbate interaction becomes more important as the coverage increases. The close packing of these adsorbed species at high coverages can alter the adsorption site, orientation, long range order, and other structural and electronic properties of the surface and near-surface regions.

Perhaps the most studied of these dense molecular overlayers is the saturation monolayer of carbon monoxide adsorbed on the Ni(110) surface at temperatures below 200K. The structure of CO/Ni(110) at various coverages has been investigated by low-energy electron diffraction (LEED),[4-7] high resolution electron energy loss spectroscopy (HREELS),[8,9] electron stimulated desorption ion angular distribution (ESDIAD),[3,10] angle-resolved photoelectron spectroscopy (ARPES),[11,12] polar X-ray photoelectron diffraction (XPD),[13,14] inverse photoemission,[15,16] and other techniques. It was observed that the CO molecules adsorb perpendicularly to the surface on a mix of top and short-bridge sites through the carbon atoms at low coverages. At coverages of 0.4 to 0.75 monolayers some of the CO molecules begin to tilt from the perpendicular orientation. As the coverage increases to near one monolayer (one CO molecule per surface Ni atom), all the CO molecules are tilted away from the surface normal, half of them towards [001] and the other half towards [00$\bar{1}$]. It was also found that the tilt angle is the same for both directions, its magnitude varying from 17°

as determined by ARPES[11] and ESDIAD[3] measurements to 21° determined with XPD. The observation of a single C-O stretch frequency also suggested that all the CO molecules occupy the same type of adsorption site.

Lambert[5] had earlier proposed a model for this structure based on its unique p(2x1)-like LEED pattern, in which the fractional order beams (±(2n+1)/2, 0) in the [1$\bar{1}$0] azimuth are absent at all energies. In this model the CO molecules are adsorbed in zigzag chains along the [1$\bar{1}$0] rows of Ni atoms, with adjacent molecules displaced alternately along the [001] and [00$\bar{1}$] directions and away from the high-symmetry sites. He also assigned the surface symmetry group as belonging to p1g1. Nishijima *et al.*[8] later suggested that this structure may be best interpreted as having p2mg symmetry because of the existence of a mirror plane along [001], which was further confirmed by experimental work using ARPES, ESDIAD, XPD and inverse photoemission.

A model of this saturation overlayer is illustrated in Figs. 1a and 1b, where we have tentatively assigned the adsorption site to be displaced short-bridge. If the CO molecules were to occupy high symmetry positions, such as undisplaced top or bridge sites, in a perpendicular fashion, the distance between these molecules would be 3.52Å in the [001] direction, but would only be 2.49Å in the [1$\bar{1}$0] direction---much smaller than the minimum intermolecular distance of 3.0-3.05Å observed for CO molecules.[1,2,17] As a result, the adjacent molecules along [1$\bar{1}$0] are tilted in opposite directions towards the [001] azimuth to avoid the strong intermolecular repulsion. Even if the CO molecules are tilted and displaced in a way such that the larger oxygen ends of the molecules are equally spaced, the O-O distances would still be only 3.05Å. This structure is in fact the most dense CO overlayer observed so far. The large dispersions of its vibrational

modes[9] and electronic energy levels[11,12] are clearly results of this densely-packed and strongly-interacting structure.

Although many experiments have been done and much has been learned about the structure and the properties of this surface layer, and the above model has been widely accepted, there are still many unknowns and much controversy concerning how the CO layer is situated above the nickel surface. Do the CO molecular zigzag chains lie along the ridges, or in the troughs of the (110) surface? If they are along the ridges, do the molecules sit on the atop sites or the short bridge sites? Would it be long bridge site or hollow site in the case where the zigzag chains lie in the troughs? How much do the CO molecules need to be displaced from these high-symmetry sites in order to minimize intermolecular repulsion? While most of the previous work on this surface did not, and was not able to, address the question of the CO adsorption site, the few studies that did differed on their conclusions about the structure. An earlier EELS study[8] favored displaced long-bridge site while a later EELS work[9] argued for a top-site adsorption by means of the more detailed symmetry analysis of the vibrational modes. A LEED I-V study,[7] on the other hand, preferred the short-bridge site adsorption and determined the carbon-metal tilt angle to be 27±5°. While the EELS method is less direct, it was pointed out that the LEED work might have ruled out the top site at too early a stage based on I-V curves for a non-tilt geometry and might have missed a possible good fit at some tilt angle. It is obvious that a more detailed investigation of this structure, possibly by another technique, was called for in order to help resolve this controversy. Another point of interest that had not been adequately addressed is how the adsorption of carbon monoxide modifies the structure of the underlying Ni substrate, particularly how it affects the Ni first- to second-layer spacing, which on a clean

Ni (110) surface was found[18] to be 1.10Å, a 10% contraction compared to 1.245Å for the bulk. The adsorption site, the carbon-nickel tilt angle and interatomic distance, and the adsorption-induced surface relaxation will be the main subjects of this report based on our investigation using angle-resolved photoemission extended fine structure (ARPEFS)[19].

There are several reasons why we use ARPEFS to study the structure of CO/Ni(110). First of all, ARPEFS is a local structural probe. It has been shown to be capable of determining surface and near-surface structures of atomic overlayers accurately, sometimes to four to five atomic layers beneath the surface.[20] Its sensitivity to both the perpendicular and the horizontal displacements of the surface layer[21,22] could be very useful for this work since the determination of the C-Ni tilt is equivalent to the determination of the lateral and perpendicular displacements of the carbon atom from a high-symmetry site on the Ni surface. Furthermore, although normal photoelectron diffraction has been used to study the adsorption of CO molecules on Ni(001) and Ni (111) surfaces[23], the technique of ARPEFS and its theoretical treatment has not been previously applied to the study of molecular overlayers on surfaces. This work would therefore be an important test of the feasibility of applying ARPEFS to the study of molecular adsorption systems.

II. EXPERIMENT

The Ni(110) crystal (7x7x1mm) used in this work was cut from a high-purity single crystal rod, then mechanically polished and chemically etched. Its orientation was determined to be within ±1° of the (110) plane using Laue backscattering. For insertion into the ultrahigh vacuum chamber the crystal was

spotwelded between two tungsten wires onto a high precision manipulator equipped with liquid nitrogen cooling. The manipulator allowed linear motions along three perpendicular axes as well as rotations about the crystal surface normal and the vertical axis. Prior to the carbon 1s ARPEFS measurement the Ni surface was cleaned by repeated cycles of Ar^+ sputtering at energies of 500 to 1000 eV, followed by annealing at 700 to 900°C with electron-beam heating. The crystal's cleanliness and surface order were monitored by Auger electron spectroscopy (AES) and LEED. After most of the bulk impurities had been segregated to the surface and removed, only one or two additional cycles of sputtering and annealing at lower temperatures (550-650°C) were needed for subsequent cleaning of the surface.

The CO overlayer was prepared by first cooling the cleaned crystal to around 120K and then backfilling the sample chamber with $1x10^{-7}$ Torr of CO through a variable leak valve filled with high purity (99.995%) CO. The storage area of the leak valve was repeatedly flushed before CO was allowed into the chamber. It was consistently observed that a p2mg(2x1) LEED pattern started to develop after an exposure of 8-10 Langmuir (L). At around 12L the pattern was very sharp, with little background. Further exposure (up to 100L) did not change either the LEED pattern or the C(273eV)/Ni(848eV) Auger peak ratio. Therefore, it was assumed that after 12L the surface reaches its saturation coverage and no further adsorption of CO occurs.

An ARPEFS experiment involves detecting the angle-resolved photoelectron intensity of a certain atomic core level as a function of electron kinetic energy in one or more directions. Therefore it requires the use of variable-energy vacuum ultra-violet or X-ray sources. For this work the experiment was performed at the National Synchrotron Light Source on beamline U3C using a 5m

extended-grasshopper-type grating monochromator. Three different experimental geometries were chosen for the ARPEFS measurements. For all the three geometries the electron emission and photon polarization directions were oriented along the [001] azimuth. In the case of simple atomic adsorption system it has been shown[24] that by aligning the electron emission direction along the bond axis linking the emitter and a backscatterer (provided a good guess can be made of the structure to be determined), the ARPEFS curves would exhibit enhanced sensitivity to these specific backscattering substrate atoms. Because the CO molecules are tilted towards the [001] azimuth, our choice of this azimuth for the photon polarization and the detection of photoelectrons was aimed to allow the structure to be determined more precisely. On the other hand, even though the two CO molecules that are tilted away in two opposite directions are chemically and structurally the same, they are not equivalent in a typical ARPEFS experiment. The measured ARPEFS spectrum is the sum of the contributions from both carbon atoms, each with its own high-sensitivity direction. Adding the two contributions effectively lowers the angular sensitivity. This complexity, in addition to the fact that neither the adsorption site for the CO molecules nor the carbon-to-nickel tilt angle can be easily guessed, left no clear choices of specific directions to make the best use of the angular sensitivity. Nevertheless, it is still very important to take ARPEFS curves at different directions to ensure that consistent structural parameters can be determined from independent measurements and to allow more meaningful estimates of errors.

The three experimental geometries, illustrated in Fig. 1c, are as follows: (a) emission at 7° off-normal towards [00$\bar{1}$] with the photon polarization vector oriented 35° from surface normal towards [001]; (b) emission and polarization both set at 27° off-normal towards [001]; and (c) emission and polarization both

at 40° from surface normal towards [001]. We will denote these three arrangements as near-normal, off-normal-1, and off-normal-2, respectively. The emission direction of geometry (a) can also be described as -7° from surface normal towards the [001] azimuth. This distinction is only important for inputs into theoretical modeling. Unless specifically pointed out, from here on we will simply use [001] to denote both the [00$\bar{1}$] and the [001] azimuths, without explicit reference to the direction of the vector.

For each of the three geometries described above the carbon 1s photoemission spectra were measured in increments of 0.08 $Å^{-1}$ (corresponding to 3-6eV depending on the kinetic energy) over the kinetic energy range of 60-400eV (photon energy in the range of 350-690eV). Each photoemission spectrum had an energy window of 20-25eV, with the photopeak appearing approximately at the center. Data were collected using an angle-resolved and rotatable electrostatic hemispherical analyzer[25] operating at 160 eV pass energy. The angular resolution of the input lens is 3°. The combined resolution of the photon source and the electron energy analyzer increases from 1.0 to 2.5eV with increasing energy. Photoemission spectra were taken right after the cleaned and cooled Ni sample was exposed to 20L of CO gas. To avoid desorption or dissociation of the CO molecules by electron bombardment, neither LEED nor Auger observations were made until after each ARPEFS curve was completed, which typically entailed 6-8 hours of measurement. Throughout the experiment the base pressure of the chamber was between $8x10^{-11}$ and $2x10^{-10}$ Torr. LEED pattern after each run showed the p2mg(2x1) symmetry with sharp spots, and no impurities were detectable with AES.

III. DATA REDUCTION

To generate photoemission partial cross sections as a function of photoelectron kinetic energy it is necessary to extract the photopeak areas of all spectra for a given geometry and normalize these areas to one another in order to compensate for the variations in the energy-dependent photon flux and the transmission function of the electron analyzer. Each photoelectron spectrum has three components, the photopeak, a energy loss function, and an inelastic background[19]. In recent ARPEFS studies[22,26] a Voigt (Gaussian convoluted with Lorentzian) function has been used to model the core-level photoelectron peak, accounting for both the lifetime broadening and the limited resolution of the photon source and the electron analyzer. The carbon 1s peaks in this study, however, showed pronounced asymmetry in its shape and cannot be accurately modeled with a Voigt function. This asymmetry in photoemission and photoabsorption line shapes has been discussed by Doniach and Šunjić[27] who attributed it to the Kondo-like many-body electron interaction of the final-state core hole with the conduction electron. Employing a Doniach-Šunjić function instead of a Voigt function to describe the carbon 1s photopeak indeed improved the modeling greatly. The other functions that are used to least-squares fit each spectrum were a Gaussian-convoluted step function to model the energy loss function and an experimental background template determined using a procedure described elsewhere.[20] Initially all parameters were allowed to vary during the fit. The values of the some of the parameters, such as the widths and asymmetry of the Doniach-Šunjić function, were then plotted against the electron kinetic energy and modeled as smooth functions using low-order polynomials. Values of these functions were in turn used as fixed values in the next round of fitting.

After a few repetitions the Lorentzian width was fixed at 0.3 eV, the asymmetry parameter at 0.15 and the Gaussian width described by a smooth monotonic function with its values varying between 1.0 and 2.5 eV over the kinetic energy range of 60-400eV.

The background template served as an excellent normalization scheme[19] and was also used to subtract carbon KLL peaks from the photoelectron spectra. The energy-dependent photoemission intensity I(E) was generated by plotting the Doniach-Šunjić peak area, divided by the coefficient of the background template, as a function of the mean energy of the peak. I(E) can be expressed as

$$I(E) = I_0(E)[1+\chi(E)], \tag{1}$$

where $I_0(E)$ is a slowly varying atomic-like partial photoemission cross section for carbon 1s and $\chi(E)$ is the rapid oscillations of this cross section due to the scattering of electrons by nearby atoms. $\chi(E)$ is the ARPEFS and can be obtained from I(E) by the removal of $I_0(E)$,

$$\chi(E) = [I(E)/I_0(E)] - 1. \tag{2}$$

$I_0(E)$ is in principle the carbon 1s atomic cross section of carbon monoxide modified by the change of chemical environment upon adsorption to the Ni surface. It can in principle be calculated theoretically. In practice it can also include other low-frequency variations resulting from our data collection and reduction procedures. Therefore a low-order polynomial was used to least-squares fit I(E) and then used as an approximation to $I_0(E)$. One way to check the validity of this procedure was to multiply I(E) by some slowly varying function

and then extract the $I_0(E)$ of this new I(E) curve as described above. The $\chi(E)$'s obtained in this manner were quite reproducible, which indicates that as long as the contributions to $I_0(E)$ are manifested as multiplication of low-frequency functions, they will have little effect on the ARPEFS curve $\chi(E)$. In other words, while the I(E) curve may include low-frequency contributions from other than scattering processes, the $\chi(E)$ curve extracted in this manner has little dependence on these contributions. This is why $\chi(E)$ instead of I(E) is used in comparing the experimental and theoretical curves in the R-factor analysis to be discussed later.

One of the consequences of the above procedure is that any ARPEFS structures that come from scattering at path-length differences (PLD) of less than around 2 Å will be eliminated or distorted. Therefore, structural parameters that would need to be calculated from these path-length differences cannot be determined accurately. Since the oxygen atoms in the CO molecules are situated above the carbon atoms, the path-length differences between the direct carbon 1s photoelectron wave and the oxygen-scattered wave measured at the detector fall within the range of 0-2Å for all the three experimental geometries described in Section II. Therefore, the C-O bond length and tilt angle cannot be independently determined from our study. However, the tilt angle has previously been determined[3,10,11,13] to be within 3-4° from 19°, as was mentioned in Section I. And since the C-O bond order is not significantly reduced upon adsorption, judging from the C-O stretch frequency of 1984 cm^{-1} as compared to 2143cm^{-1} for gas phase CO molecules, its bond length should stay within a few hundredths of an Å of the 1.13Å for gaseous carbon monoxide.[28] These uncertainties in the bond angle and bond length are about the same magnitudes as would have been possibly determined with ARPEFS. Therefore in later analysis these two

parameters will be treated as having almost known values, each with a small adjustable range.

Having extracted the ARPEFS curves $\chi(E)$ using the procedure described above, it is necessary to convert $\chi(E)$ to $\chi(k)$ for Fourier analysis, where k is the magnitude of the photoelectron wavevector inside the Ni crystal and can be calculated using the de Broglie relation:

$$k(\text{Å}^{-1}) = 0.5123[E + V_0(eV)]^{1/2}, \tag{3}$$

where V_0 is the inner potential of the solid. The exact value of V_0 is not known but is around 10 eV for nickel. It is treated as an adjustable parameter in our R-factor analysis. For the purpose of qualitative Fourier analysis we simply used 10 eV to do the conversion. The AEPEFS $\chi(k)$ curves obtained in this manner for the three experimental geometries are presented in Fig. 2.

IV. STRUCTURAL DETERMINATION

Recent ARPEFS studies[20,22,26] have employed a two-step approach to the surface structural determination using the measured $\chi(k)$ curves. Adsorption sites and approximate interatomic distances could in most cases be determined from simple Fourier analysis, while quantitative surface geometries require theoretical simulations. To understand how structural information can be extracted from the ARPEFS $\chi(k)$ curves it is useful to examine the ARPEFS equation, which in the limit of single-scattering follows the expression

$$\chi(k) = \sum_j A_j(k)\cos[kr_j(1-\cos\theta_j) + \phi_j], \tag{4}$$

where $A_j(k)$ includes the elastic scattering amplitude, thermal vibrations, inelastic scattering, and other non-structural factors; ϕ_j is the scattering phase shift; r_j is the distance between the photoemitting carbon atom and the jth scattering atom; and θ_j is the scattering angle.

a. Fourier Analysis

The sinusoidal form of $\chi(k)$ suggests that if a Fourier transformation is made of the data, the Fourier peaks should appear at the path-length differences $r_j(1-\cos\theta_j)$, shifted by some small amount if the scattering phase shift ϕ_j is energy-dependent. The shift caused by ϕ_j is usually less than 0.2 Å and can be ignored for qualitative analysis.

The Fourier spectra for the three geometries are shown in Fig. 3. There are notable similarities among the three curves. All three spectra have a dominant feature at 3-4Å. However, each one of these features is actually the overlap of many peaks at closely spaced path-length differences that are associated with scattering from the first and second layers of Ni atoms. For example, if we refer to the final results of the structural determination, the first feature in the off-normal-2 geometry can be shown to come from four major single-scattering events with path-length differences at around 2.9Å, 2.9Å, 3.3Å and 4.4Å, respectively, and about a dozen minor peaks. Some of these scattering events followed by a second scattering from the oxygen atoms may also have total path-length differences within the range of the broad feature. It is easy to see that, with two inequivalent carbon photoemitters, adsorption sites that are displaced from high-symmetry positions, and the small Ni interlayer spacing (1.245Å in the bulk), many scattering events will have very closely-spaced path-length differences. The

resolution of the above fast Fourier transformation can be estimated[29] to be no better than 1.7 Å. It would still be larger than the separation between the nearest path-length differences even with auto-regressive prediction.[29] It is therefore very difficult to pick a preferred site based on Fig. 3 alone, given that most sites could have some Fourier peaks falling in this range. It appears that, although Fourier analysis has been demonstrated to be very useful in determining surface adsorption sites and thus narrowing down parameter space for further analysis in the case of simpler systems, such as atomic adsorption in high-symmetry sites with well-spaced path-length differences, it could not be used as effectively for more complex overlayers.

b. MSSW analysis

Another way of looking at the limitation of above Fourier analysis is that it uses only half the information in the original $\chi(k)$ curves---it uses only the frequency, but not the phase. This full information is used in the second method of extracting structural information from ARPEFS curves, by means of multiple-scattering spherical-wave (MSSW) analysis. In this method the experimental curves are compared with theoretical MSSW calculations for various trial structures. The structure that results in the best agreement between the experiment and the theory is considered the most likely structure for the system of interest.

The theoretical background of MSSW has been described in great details elsewhere.[30] A MSSW calculation takes as input a set of trial structural parameters and nonstructural parameters that include atomic partial-wave phase shifts (PWPS), isotropic Debye temperatures of surface atomic layers, photon polarization and electron detection directions, analyzer aperture, mean-free path

parameters, experimental temperature, and the inner potential. The theory is most sensitive to structural parameters. Both the overall features and the more subtle details in the structure, such as corrugation and reconstruction, can be revealed with good precision.[20,22]

In the present study the nickel partial-wave phase shifts were from previous calculations.[31,26] The carbon and oxygen phase shifts were calculated with a modified program by Pendry,[32] using a potential obtained from atomic Hartree-Fock wave functions. The exchange potential was treated using the Xα approach with the α's taken from the work of Schwarz.[33] The muffin-tin radii for both atoms were varied between 0.5 and 0.8Å in the calculations and the optimum values were found to be between 0.65Å and 0.7Å. The sum of these muffin-tin radii is about 1.2 times the interatomic distance of 1.13Å for carbon monoxide. Using the phase shifts calculated at these radii gives the best fits between theoretical and experimental curves and the best consistency among results obtained from the three experimental geometries. We do not yet have a definite explanation for this "expansion". One possibility is that it is needed to account for the bonding electrons that are "shared" by both atoms in the molecule. We have also tried the *ab initio* complex partial-wave phase shifts calculated using the program by Rehr *et al.*[34,35] Structural results using these two sets of phase shifts agree very well. A full comparison will be presented in Section V.

Surface thermal vibrations were described by a correlated Debye model.[30] The nickel bulk Debye temperature was set at 375K, while its surface Debye temperature was fixed at 263K, 289K, and 263K for the [001], [1$\bar{1}$0], and [110] directions, respectively. Variations of the oxygen-layer Debye temperatures have very little effect on the carbon 1s ARPEFS curves; they were set at 500K. The

carbon Debye temperatures were initially taken at 550K for the three crystalline directions, but were allowed to vary in the calculations. The inelastic scattering was accounted for by including an exponential factor $e^{-r/\lambda}$, where $\lambda = ck$, and $c = 0.753$. The aperture size of the detector was fixed at 3° half angle. The inner potential for Ni was varied between 5 and 15eV in the fit. The experimental temperature (125±10K) and the crystal and analyzer alignments (±3°) were allowed to vary due to the limited accuracy in determining them experimentally.

For structural parameters we considered all the adsorption geometries in which the carbon atoms occupy any sites between two adjacent top sites or two adjacent short-bridge sites along the [001] azimuth, i.e., all the sites along lines AB and CD as illustrated in Fig. 4. The C-Ni interatomic distance was taken at 1.9 ± 0.2Å, and the first- to second-layer Ni distance was allowed to vary between 1.1 and 1.4 Å. The C-O bond length and tilt angle were varied in ranges of 1.10-1.20Å and 15-23°, respectively. To preserve the p2mg symmetry of the surface the two CO molecules in the unit cell were treated as having the same bond length, same C-Ni distance, and the same tilt angles. The tilt directions were towards [001] and [00$\bar{1}$], respectively. With the further constraint that the nearest oxygen-to-oxygen distance be greater than 2.8Å, or about 0.2Å shorter than has been observed to be the minimum O-O distance, the structural parameter space could be further reduced into five smaller subspaces, shown as five different structural models in Fig. 5. The choice of 2.8Å is to allow for the possible small change in the size of the CO molecules upon adsorption to the surface. These models also included some structures that were out of the ranges specified above, and some overlap of parameter space occurs among the five models, specifically between the hollow and the bridge-II sites. The important aspect is that they included <u>all</u> possibilities within the set constraints. It should be noted the top-II

site can also be classified as a long bridge site; it is designated as a top site because the carbon atom is bonded closer to one of the two long-bridge atoms.

Each of the five models was characterized by an angular range specifying the C-Ni tilt angle. In the case of the short-bridge site this angle was between the surface normal and the vector connecting carbon and the midpoint of the two nickel atoms to which the carbon atom is bonded. In the cases of top-site adsorption and hollow-site adsorption, which is actually adsorption on top of second-layer Ni, this angle is simply the tilt of the C-Ni bond from the surface normal.

To determine the geometric structure from the ARPEFS data the experimental $\chi(k)$ curves were compared with MSSW calculations using varying values for the structural and non-structural parameters until the best agreement was reached. This optimization is implemented by minimizing the R factor, defined as

$$R = \frac{\sum_i [\chi_E(k_i) - \chi_T(k_i, \{P_j\})]^2}{\sum_i \chi_E^2(k_i)} , \qquad (5)$$

where $\chi_E(k)$ is the experimentally determined ARPEFS curve, $\chi_T(k)$ is the MSSW calculation, subscript i indicates the ith data point, and $\{P_j\}$ is the set of parameters to be optimized. The k ranges were 4.2-10.0Å^{-1}, 4.5-10.1Å^{-1}, and 4.5-9.75Å^{-1} for the near-normal, off-normal-1, and off-normal-2 curves, respectively. Since we had three experimental curves and five possible structural models, there were fifteen possible experimental-theoretical combinations, each with its own parameter subspace. To minimize the R-factors for each of these combinations a simplex routine was used to automatically search both the structural and

nonstructural parameters simultaneously until a minimum R factor was reached. Different starting guesses were tried to make sure that results from the fits were reproducible.

The experimental $\chi_E(k)$ curves used in the R factor minimization were smoothed by Fourier-filtering out high-frequency noise. Residual low frequency contributions not removed by the $I_0(E)$ extraction procedure described earlier were also filtered out. The cutoffs were 1.0Å and 10.05Å, 1.0Å and 9.35Å, and 1.0Å and 10.30Å for the near-normal, off-normal-1, and off-normal-2 curves, respectively (Fig. 2). The theoretical $\chi(k)$ curves are expected to have large contributions from scattering events with low path-length differences (mainly the scatterings off oxygen atoms) and may not oscillate around zero, such as is the case for the off-normal-1 curve, illustrated in Fig. 6. To maintain consistency with the reduction procedure for the experimental data, theoretical $\chi(k)$ curves were calculated for path-length differences between zero and the high path-length-difference cutoffs mentioned above. Each $\chi(k)$ was then added to 1 to obtain I(k) [Eq.(1)], with the atomic-like cross section $I_0(k)$ assumed to be a slowly varying function (Section III)---a constant was used here. A low-order polynomial was then used to extract $I_0'(k)$, which now includes low-frequency oscillations from scattering. A modified $\chi'(k)$ was then constructed using Eq.(2). After Fourier-filtering out the residual low-frequency part we now had the $\chi_T(k)$ used in Eq.(5).

Results of the best fits for the fifteen combinations are summarized in Table I. The partial-wave phase shifts used in these fits are those of our calculations described earlier in this section. Comparisons between experimental and theoretical $\chi(k)$ curves are shown in Figs. 7a-7e. From Table I it is clear that the short-bridge site represents the most probable adsorption site for carbon monoxide. Not only are the agreements between the experiment and the theory

best for this site, with the lowest R factors, but the final structural and non-structural parameters determined from the three curves taken at different directions are also the most consistent for adsorption on this site. For the other structural models, although the agreement in the main frequencies between the experimental and the theoretical $\chi(k)$ curves may look reasonable for some of the curves in Figs. 7a-7e, the amplitudes do not match well. Furthermore, parameters determined from the three curves do not match. Had we required each parameter to take the same value for all three curves, the R factors for all but the bridge sites would have been significantly larger. Our analysis therefore points out to the importance of taking multiple $\chi(k)$ curves at different directions, especially for complicated systems for which qualitative structural information cannot be obtained from Fourier analysis.

While the Fourier-transform method discussed in Section IV.a was not used to determine the surface structure, we did Fourier-transform all the above best-fit theoretical $\chi(k)$ curves and compare them with the experimental curves. The results are plotted in Figs. 8a-8e. The MSSW calculations for the Bridge-I structure gave Fourier-transform curves in very good agreement with experiment, while the Fourier transform for the other trial structures showed poor agreement. This constitutes good confirmatory evidence for the adopted structure.

V. ERROR ANALYSIS

To illustrate the sensitivity of ARPEFS structural determinations we plot the R factor as functions of the C-Ni tilt angle, the C-Ni interatomic distance, and the Ni first- to second-layer distance, shown in Fig. 9. All parameters except the abscissas are fixed at their optimal values. It is quite obvious that the three $\chi(k)$

curves have about the same sensitivities to each structural parameter, quite unlike previous ARPEFS studies where directional sensitivities were used to highlight certain backscattering atoms. This is not unexpected since many more important scattering events contribute to the total $\chi(k)$ curve because of this system's structural complexity.

The statistical error associated with each structural parameter for a given $\chi(k)$ curve can also be estimated from Fig. 9. Since our R factor minimization is in essence a nonlinear least-squares fit, we shall use the χ^2 method[36] in the following error analysis. Using the same notations as in Eq.(5), χ^2 is defined as

$$\chi^2 = \sum_i \frac{[\chi_E(k_i) - \chi_T(k_i)]^2}{\sigma_i^2} , \tag{6}$$

where σ_i is the variance of the ith data points. [Notice that χ^2 is to be treated as a symbol here to comply with convention and should not be confused with $\chi(k)$.] In the absence of good independent estimates of σ_i we assume that[36]

$$\sigma_i^2 \approx \sigma^2 \approx s^2 = \frac{1}{N-n} \sum_i [\chi_E(k_i) - \chi_T(k_i, \{P_j\})]^2_{min} , \tag{7}$$

where N is the number of independent data points in a given $\chi_E(k)$ curve, n is the number of parameters used in the fit, and the subscript "min" indicates that optimized values of the parameters P_j are used in the summation. Using the Nyquist sampling theorem[37] we estimate that $N = (\Delta k \cdot \Delta r) / \pi$, where Δk is the data range and Δr is the range of path-length difference used to filter the experimental data.

In making the assumption of Eq. (7) we do not have an independent assessment of the goodness of fit in the R-factor analysis. However, the statistical error of each structural parameter can still be estimated by

$$\sigma_{P_j}^2 = \frac{2}{\frac{\partial^2 \chi^2}{\partial P_j^2}} \quad . \tag{8}$$

In terms of R-factor Eq.(8) becomes

$$\sigma_{P_j}^2 = \frac{2}{\frac{\partial^2 R}{\partial P_j^2}} \times \frac{R_{min}}{N-n} , \tag{9}$$

where R_{min} is the lowest R factor for the given curve. The partial derivative $\partial^2 R/\partial P_j^2$ is the curvature of the R versus P_j plot near the vicinity of lowest R factor and is obtained by fitting a parabola to the data.

Results of the errors estimated using Eq.(9) are listed in parentheses in Table II. Columns 2-4 gives the statistical errors associated with each parameter for the three data sets. Column 5 lists the weighted average and weighted uncertainty of each parameter, while column 6 lists the simple average and standard deviation of each parameter calculated from the scatter of its value among the three curves, without using the estimated errors from columns 2-4. Listed in Column 7 are the final structural parameters that we assign to this system, with the values taken from column 5 and the errors from the greater of columns 5 and 6, which in this case turn out to be the errors listed in column 6. The fact that the parameter values are more scattered among the three curves than their *statistical* errors (column 5) would suggest is probably an indication of the

existence of *systematic* errors that tend to affect different $\chi(k)$ curves differently. The errors listed in column 6 therefore reflect these errors to a certain extent.

Systematic errors could arise from both experimental and theoretical sources. Experimentally these sources may include the misalignment of the crystal, the electron detector, and the photon beams. The error could also arise from the $I_0(E)$ removal procedure described in Section III. These errors are generally quite small and are further reduced if the relative alignment is allowed to vary within experimental accuracy in the R-factor analysis, and if both experimental and theoretical curves are Fourier filtered identically.

Theoretical sources of error in principle include all approximations used in modeling the scattering of electron in the solid. The major source, however, is the partial-wave phase shifts used in the MSSW calculation. Because of the angular dependence of the total scattering amplitude and scattering phase that are calculated from the partial-wave phase shifts, the resulting errors could be different for the $\chi(k)$ curves measured in different directions. By varying the muffin-tin radii until the resulting atomic phase shifts give the best agreement among the three curves (Section IV.b), we hoped to at least partly reduce the errors from the scatter of parameter values. However, the underlying theoretical approximation of atomic scattering potential used in various phase-shift programs could also cause the derived structural parameters to be biased either high or low for most or all of the curves, thereby giving rise to higher or lower final interatomic distances and other structural parameters. It has been estimated[39] that the derived nearest-neighbor distances could in some cases vary by as much as 0.02-0.03 Å using phase shifts calculated from various sources.

Much effort has been made to improve the phase shift calculation by adopting better approximations to the atomic charge densities and atomic

potentials. The recent theoretical work of Rehr *et al.*[34,35] has been very successful in modeling EXAFS data to an accuracy of better than 0.02Å for nearest-neighbor distances. Their *ab initio* phase shift calculations require only inputs of atomic numbers, interatomic distance, and coordination numbers. To arrive at some estimate of the possible bias in our structural determination we have used their program to calculate the phase shifts, and used these phase shifts in an independent R-factor analysis for the bridge-I adsorption geometry. The results are listed in Table III, along with the estimated errors using the procedure described earlier in this section. The $\chi(k)$ curves are plotted in Fig. 7f and the Fourier-transform curves plotted in Fig. 8f.

Comparing Table II and Table III one finds excellent agreements between the structural parameters determined using the two sets of partial-wave phase shifts. A close examination reveals generally larger C-Ni tilt angles, shorter C-Ni bond lengths and larger first- to second-layer Ni distances using the phase shifts of Rehr *et al.*, with the differences averaging 0.01Å for distance and 1° for tilt angle. (The weighted averages of Ni interlayer spacing are both reported as 1.27Å due to round-offs.) The error associated with each parameter and the best R-factor are also very close for both sets of phase shifts. The optimal inner potentials are lower using Rehr's phase shifts, but the relative magnitudes among the three data sets remain little changed. Given that different theoretical approaches were used to describe the atomic potential that is used in the calculations of the two sets of phase shifts, the agreement is indeed very good. Small systematic biases may exist in our structural results, but they should not be greater than the estimated statistical and random errors.

Although we have shown that both sets of phase shifts result in the same structure, the program by Rehr *et al.* has apparent advantages. With a more

complete theoretical model that takes into account the atomic coordination and chemical environment, it eliminates the tedious and somewhat arbitrary procedure of searching for the optimal muffin radii in the phase shift calculations. This is particularly important for molecules like CO because an isolated atomic potential model does not adequately address the effect of the valence bonding electrons on the atomic scattering potential. For atomic adsorption the choice of muffin-tin radii was shown to affect the structural determination to a lesser degree.[31,20-22,38]

VI. DISCUSSION AND CONCLUSION

The optimized structure of a saturated overlayer of CO molecules on the Ni(110) surface is illustrated in Fig. 10. The values listed in Table II are chosen as the final structural parameters, although the results listed in Tables II and III are almost identical. Our detailed analysis strongly favors the tilted short-bridge site for the adsorbed CO molecules. The C-Ni interatomic distance is 1.94(0.02)Å, with the two adjacent carbon atoms along the $[1\bar{1}0]$ zigzag chain displaced from their ideal bridge sites along the [001] and $[00\bar{1}]$ directions, respectively. The C-Ni tilt angle projected onto the (001) plane, or the angle between the surface normal and the vector connecting the carbon atom and the midpoint of the two Ni atoms to which the carbon is bonded to, is 16(2)°. The displacement of carbon from the ideal bridge site is 0.41(0.05)Å. The first- to second-layer spacing of nickel increases from 1.10Å for clean Ni(110) surface[17] to 1.27(0.04)Å upon the adsorption of CO molecules, probably because the chemical bond between the carbon atom and the first layer Ni atom weakens the Ni-Ni bond. The value of 1.27Å is very close to the bulk Ni interlayer spacing of 1.25Å.

The C-O bond length and tilt angle cannot be independently determined from this study. The main reason for our inability to locate the position of the oxygen atoms is that they are situated above the carbon photoemitters. The path-length differences for the scattering of photoelectrons from the oxygen atoms are therefore small, and would show up as very low-frequency modulations in the $\chi(k)$ curves. These low-frequency modulations are either removed or distorted during the data reduction, and cannot be used for reliable structural determination. Fortunately, the CO bond length and tilt angle had been obtained or inferred with good precision by other studies. These predetermined values were used in the R-factor optimization, as discussed in Sections III and IV.b. They were allowed to vary along with the other parameters, but they were varied only through the limited ranges of 1.10-1.20Å and 15-23°, as noted in Section IV.b, thereby covering the values reported from previous studies. As expected, the R-factors were less sensitive to these two parameters, which affected mainly the amplitude of the $\chi(k)$ curves because of forward scattering through the oxygen atoms, but nonetheless optimized values were obtained. For the Bridge-I structure the optimal values from the fitting of the three experimental $\chi(k)$ curves all fell within the ranges of 1.15-1.18Å and 18.5-20.5°, with averages at 1.16Å and 19°, respectively. Error limits do not follow readily from this approach, but if we conservatively take the errors equal to the entire ranges through which the CO bond length and tilt angle were varied in the R-factor analysis, or ±.05Å and ±4°, respectively, then the shift of oxygen from carbon along the [001] direction can then be calculated as 0.38(0.08)Å, for a total oxygen-atom displacement of 0.79(0.09)Å from the ideal "vertical" short-bridge site.

We discussed in Section I that the main reason the CO molecules are shifted towards the [001] and [00$\bar{1}$] azimuths is to avoid the strong repulsive

force among these molecules, especially the larger oxygen end, in the [1$\bar{1}$0] direction. Assuming all the oxygen atoms are separated by equal distance, which can be shown to be 3.05Å for this system, the displacement of the oxygen atoms from the bridge site would have to be 0.88Å. Our value of 0.79(0.09)Å would produce a distance of 2.95(0.02)Å between the two closest oxygen atoms for CO molecules adsorbed on the same Ni [1$\bar{1}$0] row and 3.16(0.02)Å between the two closest oxygen atoms in adjacent rows. The nearest C-C distance can also be estimated to be 2.62Å. These numbers compare well to those shown in Fig. 1a.

Our conclusion that the CO molecules are adsorbed on the displaced bridge sites is in disagreement with the HREELS work[9] of Voigtländer *et al.* who proposed the CO molecules should occupy the displaced top sites, but agrees with the LEED study of Hannaman and Passler[7] who favored the displaced short bridge sites. However, the C-Ni tilt angle of 27(5)° determined by the LEED study is 11° greater than the 16(2)° from our study. This difference is greater than the uncertainties of both experiments. It is interesting to note that from the LEED study, the nearest O-O distance is 3.21Å for CO molecules adsorbed to the same Ni [1$\bar{1}$0] row and 2.91Å for CO molecules in the adjacent rows, almost opposite our results. This difference is illustrated in Fig.11. The smallest lateral separation between oxygen atoms in the [001] direction is 2×0.79Å from this work, separating oxygen atoms on the same Ni-atom row, and 2×0.75Å from the LEED study, separating oxygen atoms on adjacent rows. Both values agree well with the 2×0.74Å proposed by a recent He-diffraction study.[40]

ACKNOWLEDGMENTS

This work was supported by the Director, Office of Energy Research, Office of Basic Energy Sciences, Chemical Sciences Division of the U.S. Department of

Energy under Contract No. DE-AC03-76SF00098. The experiments were performed at the National Synchrotron Light Source at Brookhaven National Laboratory, which is supported by the U.S. Department of Energy's Office of Basic Energy Sciences. We are grateful to R. Gaylord for his assistance at NSLS and to J. Rehr for providing the FEFF program for the calculation of complex partial-wave phase shifts.

REFERENCES

1. P. Uvdal, P.-A. Karlssson, C. Nyberg, and S. Andersson, Surf. Sci. **202**, 167 (1988).
2. M.I. Ban, M.A. van Hove, and G.A. Somorjai, Surf. Sci. **185**, 355 (1987).
3. W. Riedl and D. Menzel, Surf. Sci. **163**, 39 (1985).
4. H.H. Madden, J. Kuppers and G. Ertl, J. Chem. Phys. **58**, 3401 (1973).
5. R.M. Lambert, Surf. Sci. **49**, 325 (1975).
6. R.J. Behm, G. Ertl, and V. Penka, Surf. Sci. **160**, 387 (1985).
7. D.J. Hannaman and M.A. Passler, Surf. Sci. **203**, 449 (1988).
8. M. Nishijima, S. Masuda, Y. Sakisaka, and M. Onchi, Surf. Sci. **107**, 31 (1981).
9. B. Voigtländer, D. Bruchmann, S. Lehwald, and H. Ibach, Surf. Sci. **225**, 151 (1990).
10. J. Lee, J. Arias, C. Hanrahan, R. Martin, H. Metiu, C. Klauber, M.D. Alvey, and J.T. Yates, Jr., Surf. Sci. **159**, L460 (1985); M. Alvey, M.J. Dresser, and J.T. Yates, Jr., Surf. Sci. **165**, 447 (1986).
11. H. Kuhlenbeck, M. Neumann, and H.-J. Freund, Surf. Sci. **173**, 194 (1986).
12. H. Kuhlenbeck, H.B. Saalfeld, U. Buskotte, M. Neumann, H.-J. Freund, and E.W. Plummer, Phys. Rev. B **39**, 3475 (1989).
13. D.A. Wesner, F.P. Coenen, and H.P. Bonzel, Phys. Rev. Lett. **60**, 1045 (1988),
14. D.A. Wesner, F.P. Coenen, and H.P. Bonzel, Phys. Rev. B **39**, 10770 (1989),
15. H.-J. Freund, J. Rogozik, V. Dose, and M. Neumann, Surf. Sci. **175**, 651(1986).
16. N. Memmel, G. Rangelov, E. Bertel, V. Dose, K. Kometer, and N. Rosch, Phys. Rev. Lett. **63**, 1884 (1989).
17. M.L. Xu and S.Y. Tong, Phys. Rev. B **31**, 6332 (1985).
18. P. Chini, Gazz. Chim. Ital. **109**, 225 (1979).
19. J.J. Barton, C.C. Bahr, S.W. Robey, Z. Hussain, E. Umbach, and D.A. Shirley,

Phys. Rev. B **34**, 3807 (1986).

20. L.J. Terminello, X.S. Zhang, Z.Q. Huang, S.Kim, A.E. Schach von Wittenau, K.T. Leung, and D.A. Shirley, Phys. Rev. B **38**, 3879 (1988).
21. L.J. Terminello, K.T. Leung, Z.Hussain, T. Hayashi, X.S. Zhang, and D.A. Shirley, Phys. Rev. B **41**, 12787 (1990).
22. A.E. Schach von Wittenau, Z. Hussain, L.Q. Wang, Z.Q. Huang, and D.A. Shirley, Phys. Rev. B **45**, 13614 (1992).
23. S.D. Kevan, R.F. Davis, D.H. Rosenblatt, J.G. Tobin, M.G. Mason, D.A.Shirley, C.H. Li and S.Y. Tong, Phys. Rev. Lett. **46**, 1629 (1981).
24. J.J. Barton, C.C. Bahr, Z. Hussain, S.W. Robey, J.G. Tobin, L.E. Klebanoff and D.A. Shirley, Phys. Rev. Lett. **51**, 272 (1983).
25. S.D. Kevan, Ph.D. thesis, University of California, Berkeley, 1980.
26. L.Q. Wang, Z. Hussain, Z.Q. Huang, A.E. Schach von Wittenau, D.W. Lindle, and D.A. Shirley, Phys. Rev. B **44**, 13711 (1991).
27. S. Doniach and M. Sunjic, J. Phys. C **3**, 285 (1970).
28. F.A. Cotton and G. Wilkinson, Advanced Inorganic Chemistry (Wiley-Interscience, New York, 1972), Chap. 3.
29. J.J. Barton, Ph.D. thesis, University of California, Berkeley, 1985.
30. J.J. Barton, S.W. Robey, and D.A. Shirley, Phys. Rev. B **34**, 778 (1986).
31. S.W. Robey, J.J. Barton, C.C. Bahr, G. Liu, and D.A. Shirley, Phys. Rev. B **35**, 1108 (1987).
32. J.B. Pendry, *Low Energy Electron Diffraction* (Academic, London, 1974).
33. K. Schwarz, *Phys. Rev.* B **5**, 2466 (1972).
34. J.J. Rehr, J. Mustre de Leon, S.I. Zabinsky and R.C. Albers, J. Am. Chem. Soc. **113**, 5135 (1991).

35. J. Mustre de Leon, J.J. Rehr, S.I. Zabinsky and R.C. Albers, Phys. Rev. B **44**, 4146 (1991).

36. P.R. Bevington, *Data Reduction and Error Analysis for the Physical Sciences* (Mcgraw-Hill, New York, 1969).

37. F.W. Lytle, D.E. Sayers and E.A. Stern, Physica B **158**, 701 (1988).

38. L.Q. Wang, A.E. Schach von Wittenau, Z.G. Ji, L.S. Wang, Z.Q. Huang and D.A. Shirley, Phys. Rev. B **44**, 1292 (1991).

39. Yu Zheng and D.A. Shirley, private communication.

40. G. Parschau and K.H. Rieder, Surf. Sci. Lett. **257**, L628 (1991).

Table I: Summary of the results of R-factor analysis for different trial models.

Geometry	Emission direction	C-(Ni) tilt angle (degrees)	C-Ni distance (Å)	Ni_1 to Ni_2 distance (Å)	Inner potential (eV)	R-factor
Bridge-I	near-normal	15	1.93	1.26	12.9	0.08
	off-normal-1	19	1.93	1.24	12.5	0.11
	off-normal-2	16	1.96	1.31	13.6	0.09
Hollow	near-normal	26	1.76	1.35	10.8	0.40
	off-normal-1	9	2.05	1.27	5.0	0.39
	off-normal-2	6	1.91	1.18	15.0	0.56
Bridge-II	near-normal	43	1.91	1.30	5.0	0.57
	off-normal-1	75	1.76	1.21	5.0	0.26
	off-normal-2	47	1.93	1.12	7.0	0.20
Top-I	near-normal	15	2.05	1.19	7.1	0.31
	off-normal-1	28	1.97	1.26	15.0	0.34
	off-normal-2	16	1.83	1.33	15.0	0.20
Top-II	near-normal	42	1.94	1.21	15.0	0.38
	off-normal-1	28	1.97	1.26	15.0	0.34
	off-normal-2	29	2.01	1.32	9.8	0.29

Table II. Summary of selected parameters determined from MSSW analysis using the complex partial-wave phase shifts calculated from our calculations (Sec. IV.b). The uncertainties are listed in parentheses.

	near-normal	off-normal-1	off-normal-2	avg[a] (stat)	avg[b] (scat)	assigned value
C-Ni tilt angle (degrees)	15(2)	19(2)	16(1)	16(1)	17(2)	16(2)
C-Ni bond length (Å)	1.93(.01)	1.93(.02)	1.96(.02)	1.94(.01)	1.94(.02)	1.94(.02)
Ni_1-Ni_2 spacing (Å)	1.26(.02)	1.24(.03)	1.31(.03)	1.27(.02)	1.27(.04)	1.27(.04)
Inner potential (eV)	12.9	12.5	13.6			
Best R-factor	0.08	0.11	0.09			

a) Weighted average and weighted uncertainty.

b) Simple average and standard deviation calculated from the scatter of results.

Table III. Summary of selected parameters determined from MSSW analysis using the complex partial-wave phase shifts calculated from Rehr's program. The uncertainties are listed in parentheses.

	near-normal	off-normal-1	off-normal-2	avg[a] (stat)	avg[b] (scat)	assigned value
C-Ni tilt angle (degrees)	17(1)	20(2)	16(1)	17(1)	18(2)	17(2)
C-Ni bond length (Å)	1.93(.01)	1.92(.02)	1.95(.02)	1.93(.01)	1.93(.02)	1.93(.02)
Ni_1-Ni_2 spacing (Å)	1.25(.02)	1.27(.03)	1.31(.03)	1.27(.02)	1.28(.03)	1.27(.03)
Inner potential (eV)	11.5	10.2	12.2			
Best R-factor	0.08	0.13	0.11			

a) Weighted average and weighted uncertainty.

b) Simple average and standard deviation calculated from the scatter of results.

FIGURE CAPTIONS

Figure 1. Schematic of the structure of p2mg(2x1)CO/Ni(110) and the experimental geometries. (a) Top view of the surface with the carbon and oxygen atoms drawn in their van der Waals sizes (Ref. 18). (b) Side view of the hard-sphere model of this overlayer. (c) The three experimental geometries for which the $\chi(k)$ curves were measured. In the near-normal geometry the photon polarization direction (not shown) is 35° from surface normal towards [001]. For the off-normal-1 and off-normal-2 geometries the photon polarization directions are the same as the directions of electron detection.

Figure 2. Experimental $\chi(k)$ curves. The darker curves represent filtered data. The lower cutoffs are 1Å for all three curves. The higher cutoffs are 10.05Å, 9.35Å, and 10.30Å for the near-normal, off-normal-1, and off-normal-2 curves, respectively. Also see Fig. 3.

Figure 3. Fourier transformation of the three raw $\chi(k)$ curves shown in Fig. 2. The three Fourier spectra are plotted on the same scale. The vertical bars near 10Å indicate the high-frequency cutoffs for the filtered data shown in Fig. 2.

Figure 4. This figure illustrates the CO adsorption sites considered in the search for the optimal structure. They are all the sites between the two ideal top sites, A and B, and all the sites between the two ideal short-bridge sites, C and D.

Figure 5. Reduced structural models based on Fig. 4 and on the parameter ranges discussed in Sec. IV.b. Figs. (a)-(c) and Figs. (d)-(e) illustrate the transition from point C to point D and from point A to point B (Fig. 4), respectively. [Notice that significant overlap occurs between (b) and (c).] The ranges of the carbon-nickel tilt angle α for these models are also shown.

Figure 6. This figure illustrates the procedure for reducing theoretical χ curves. The calculated curve $\chi(k)$ is converted to $\chi'(k)$ [$\chi'(k)=I(k)/I_0'(k)-1$], which oscillates around zero and is used to compare with an experimental curve that also oscillates around zero.

Figure 7. (a)-(e) Comparison between experimental $\chi(k)$ curves and best-fit MSSW calculations for the structural models shown in Fig. 5. The structural parameters used to generate the theoretical curves are listed in Table I. (f) Best-fit $\chi(k)$ curves for the structure in Fig. 5a using Rehr's partial-wave phase shifts (Ref. 34&35). Experimental $\chi(k)$ curves do not line up exactly for the different models because the optimized inner potentials are different (Eq. 3). The solid lines are experimental data and the dashed lines are MSSW calculations.

Figure 8. Fourier transform of the $\chi(k)$ curves in Fig. 7. The solid lines are experimental data and the dashed lines are MSSW calculations.

Figure 9. Values of the R-factor as functions of C-Ni tilt angle, C-Ni distance, and first- to second-layer Ni spacing.

Fig.10. Optimized structure of p2mg(2x1)CO/Ni(110).

Fig.11. Comparison of the structures obtained from this wrok (a) and the LEED study of Hannaman and Passler (b) (Ref. 7).

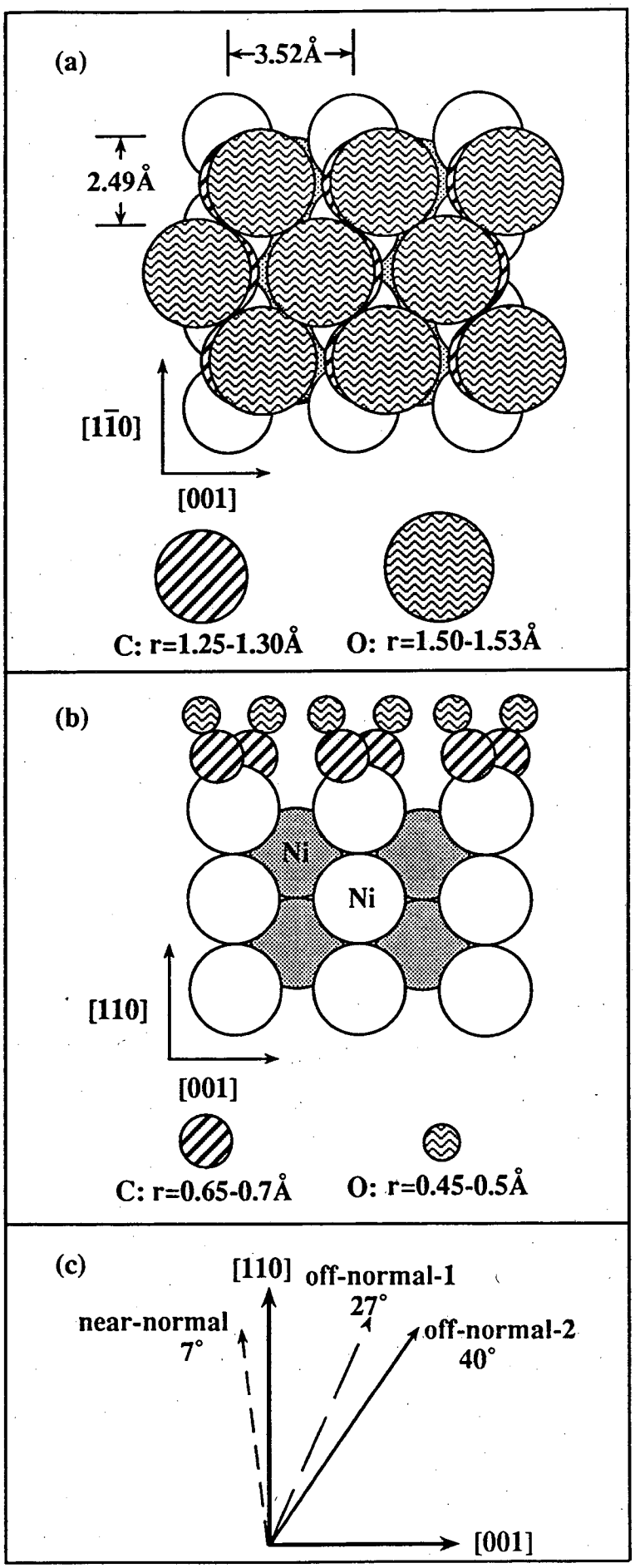
(a)
3.52Å
2.49Å
[1$\bar{1}$0]
[001]
C: r=1.25-1.30Å
O: r=1.50-1.53Å
(b)
Ni
Ni
[110]
[001]
C: r=0.65-0.7Å
O: r=0.45-0.5Å
(c)
[110]
off-normal-1
27°
near-normal
7°
off-normal-2
40°
[001]

FIGURE 1

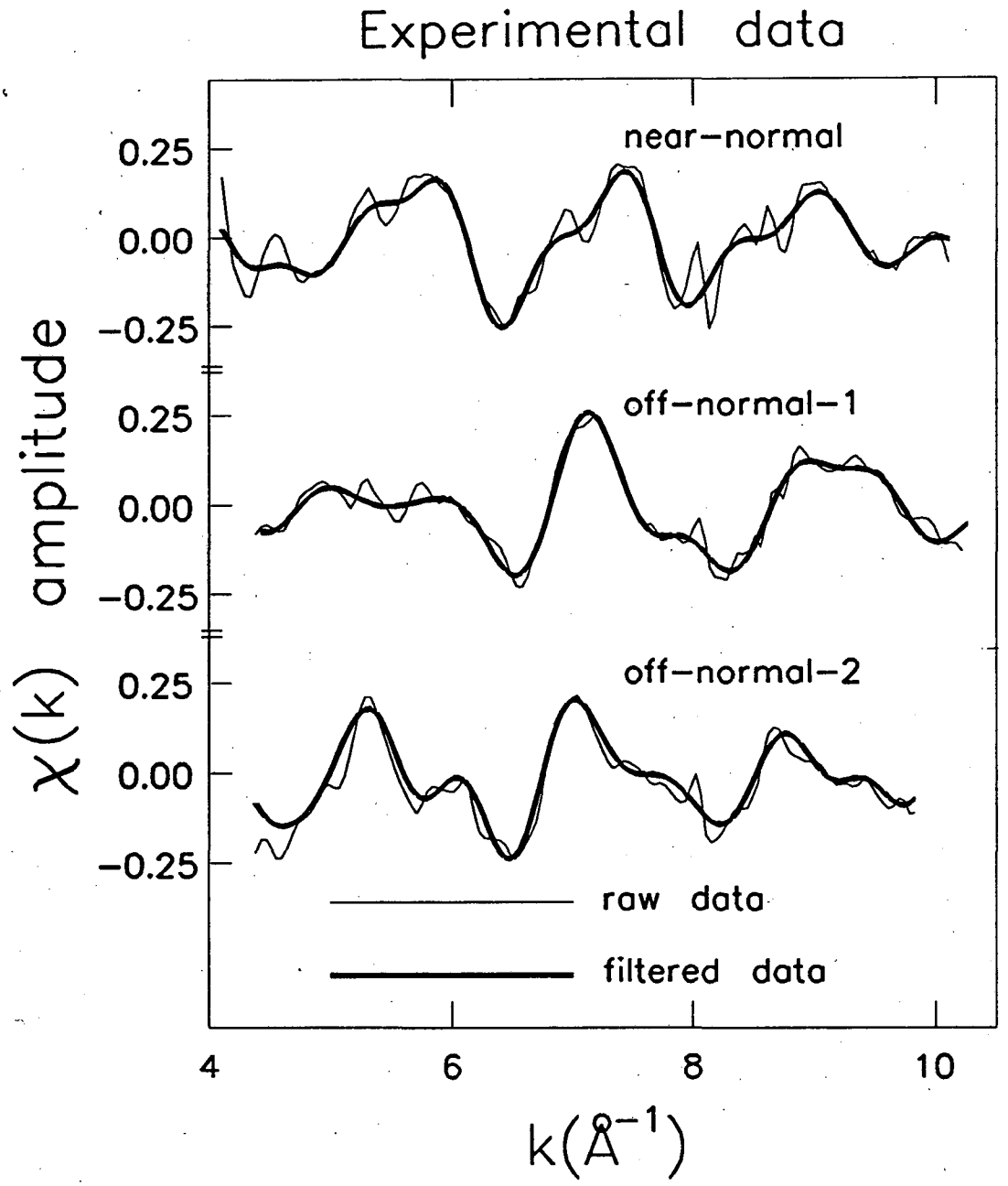
Experimental data
near-normal
off-normal-1
off-normal-2
0.25
0.00
-0.25
χ(k) amplitude
raw data
filtered data
4
6
8
10
k(Å⁻¹)

FIGURE 2

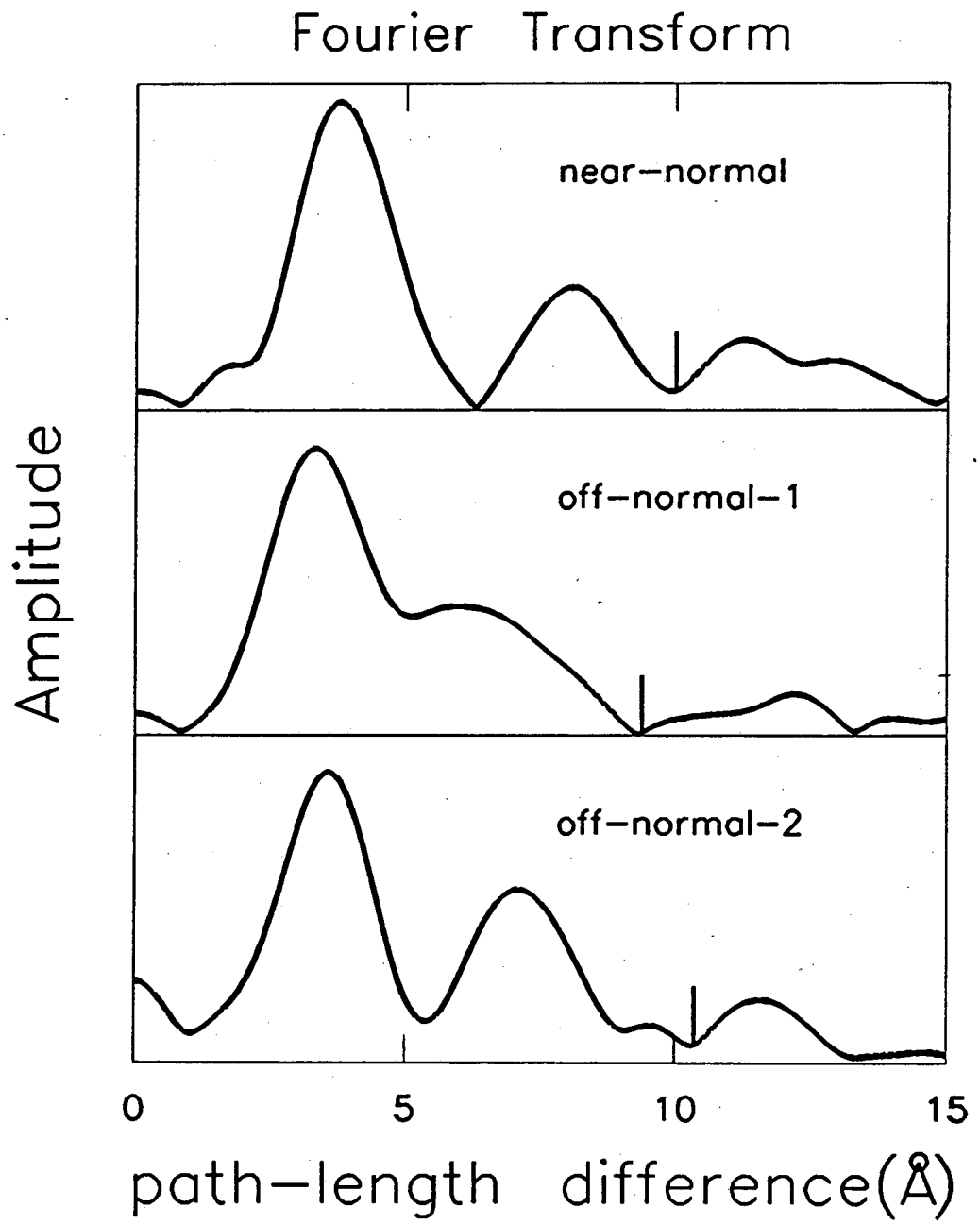
Fourier Transform
near–normal
off–normal–1
off–normal–2
Amplitude
0
5
10
15
path–length difference(Å)

FIGURE 3

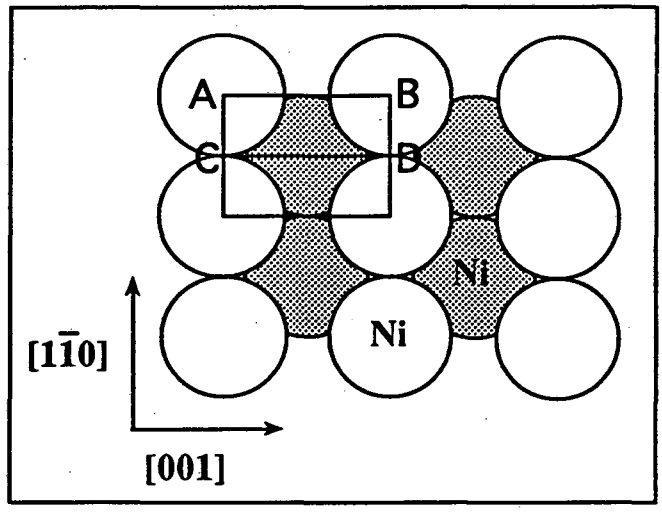

FIGURE 4

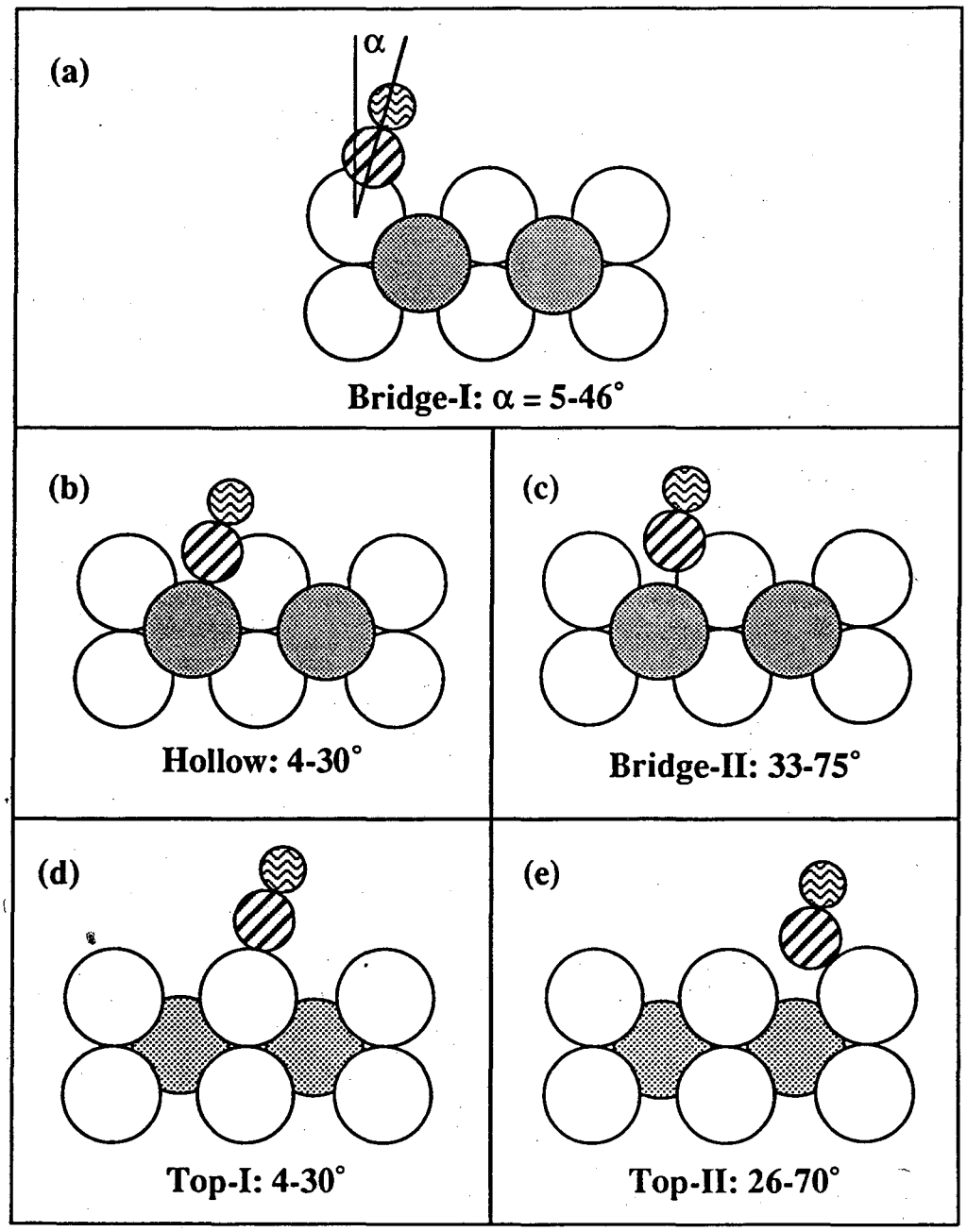
(a)
α
Bridge-I: α = 5-46°
(b)
Hollow: 4-30°
(c)
Bridge-II: 33-75°
(d)
Top-I: 4-30°
(e)
Top-II: 26-70°

FIGURE 5

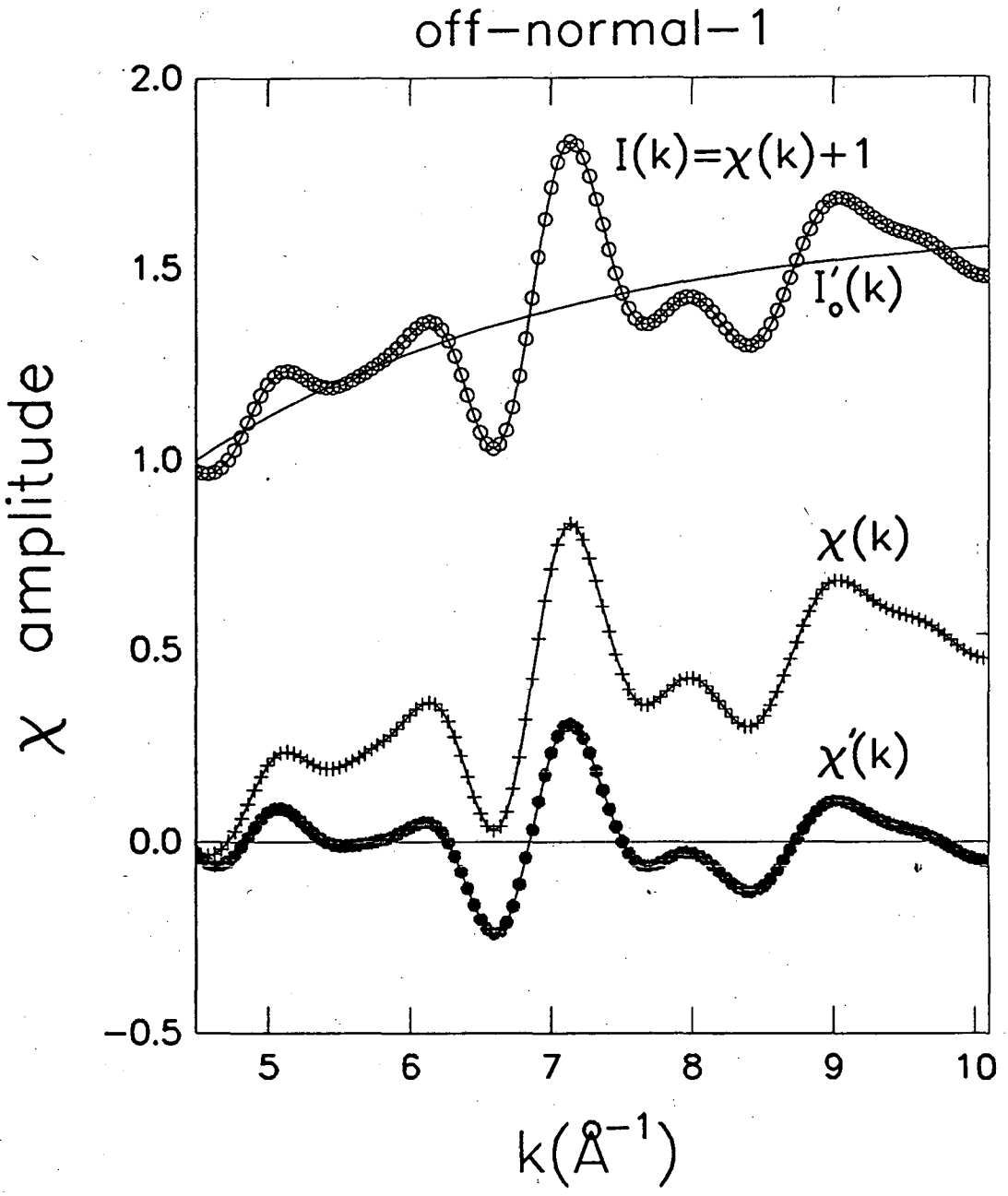
off−normal−1
2.0
1.5
1.0
0.5
0.0
−0.5
χ amplitude
I(k)=χ(k)+1
I'o(k)
χ(k)
χ'(k)
5
6
7
8
9
10
k(Å−1)

FIGURE 6

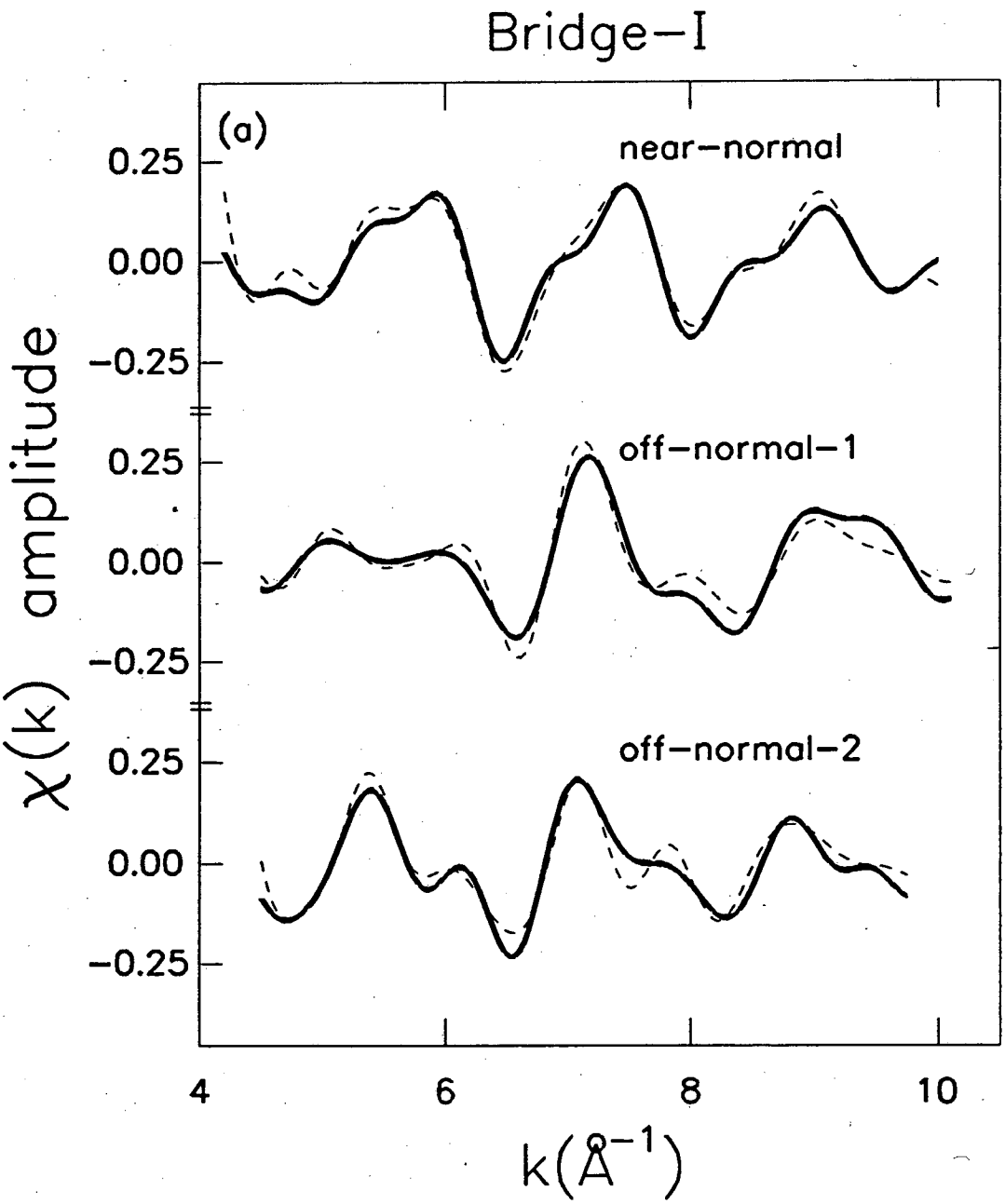
Bridge–I
(a)
near–normal
off–normal–1
off–normal–2
0.25
0.00
−0.25
0.25
0.00
−0.25
0.25
0.00
−0.25
χ(k) amplitude
4
6
8
10
k(Å^{-1})

Figure 7(a)

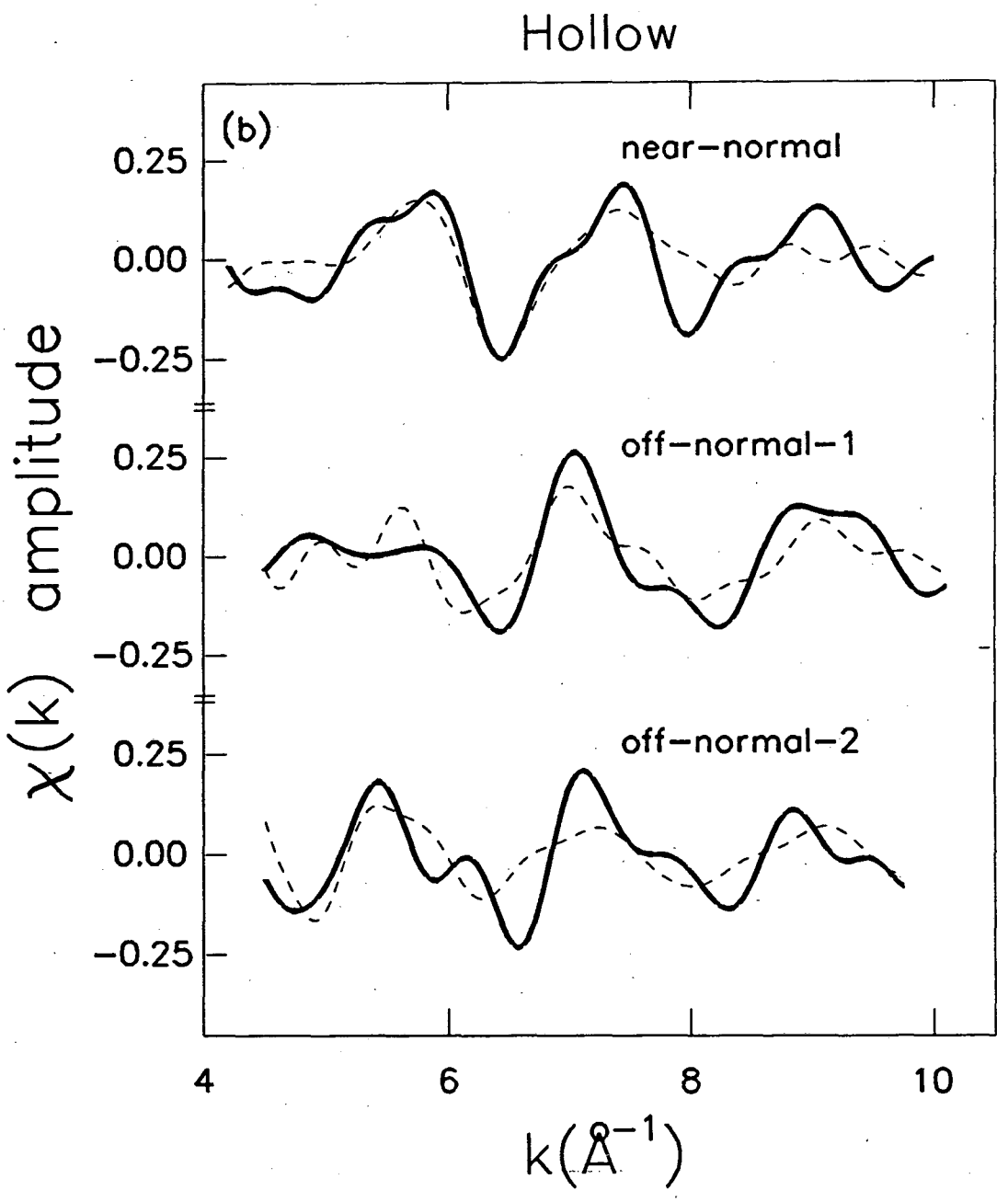
Hollow
(b)
near-normal
off-normal-1
off-normal-2
0.25
0.00
-0.25
0.25
0.00
-0.25
0.25
0.00
-0.25
χ(k) amplitude
4
6
8
10
k(Å^{-1})

FIGURE 7(b)

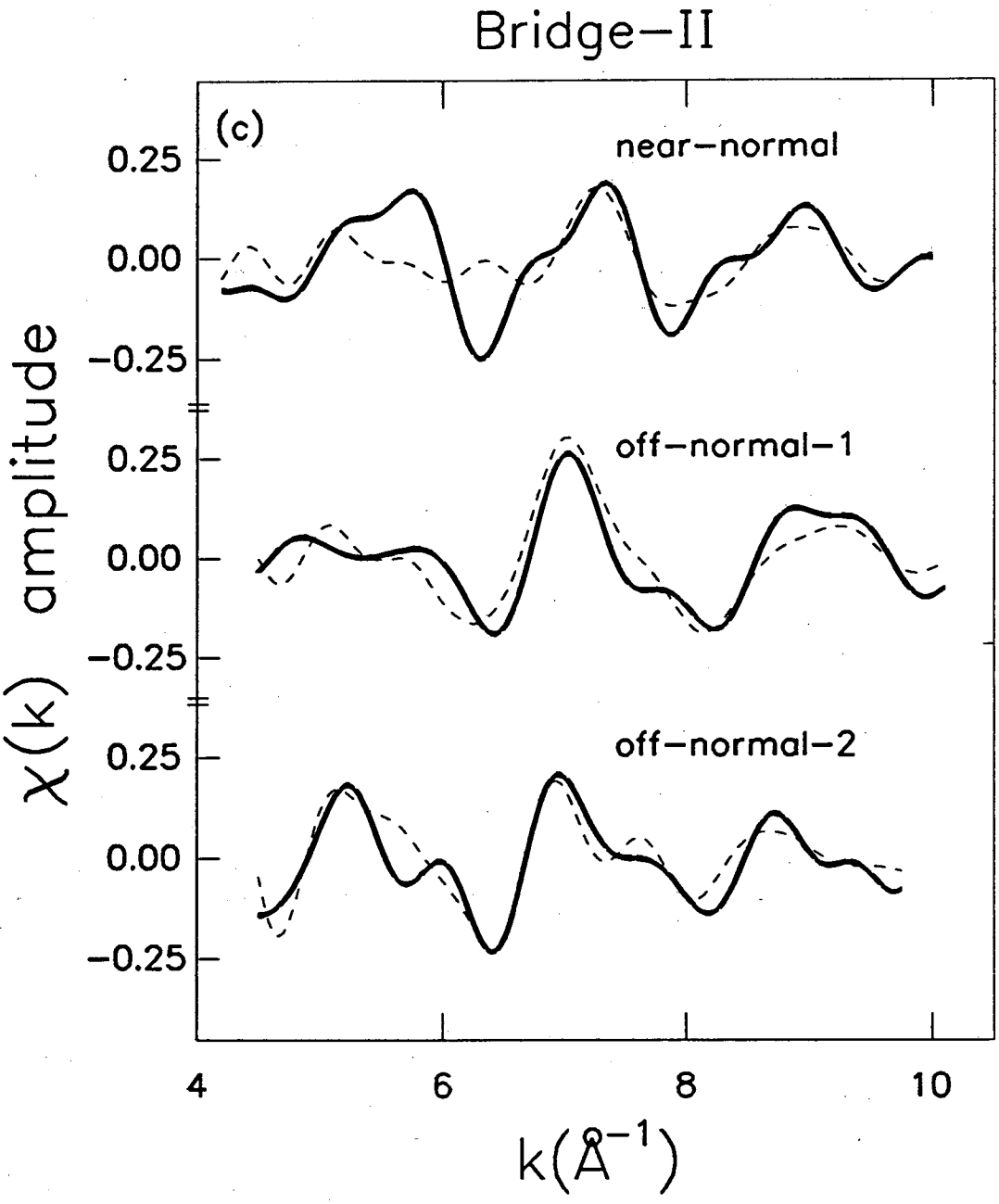
Bridge–II
(c)
near–normal
off–normal–1
off–normal–2
χ(k) amplitude
0.25
0.00
−0.25
0.25
0.00
−0.25
0.25
0.00
−0.25
4
6
8
10
k(Å^{-1})

FIGURE 7(c)

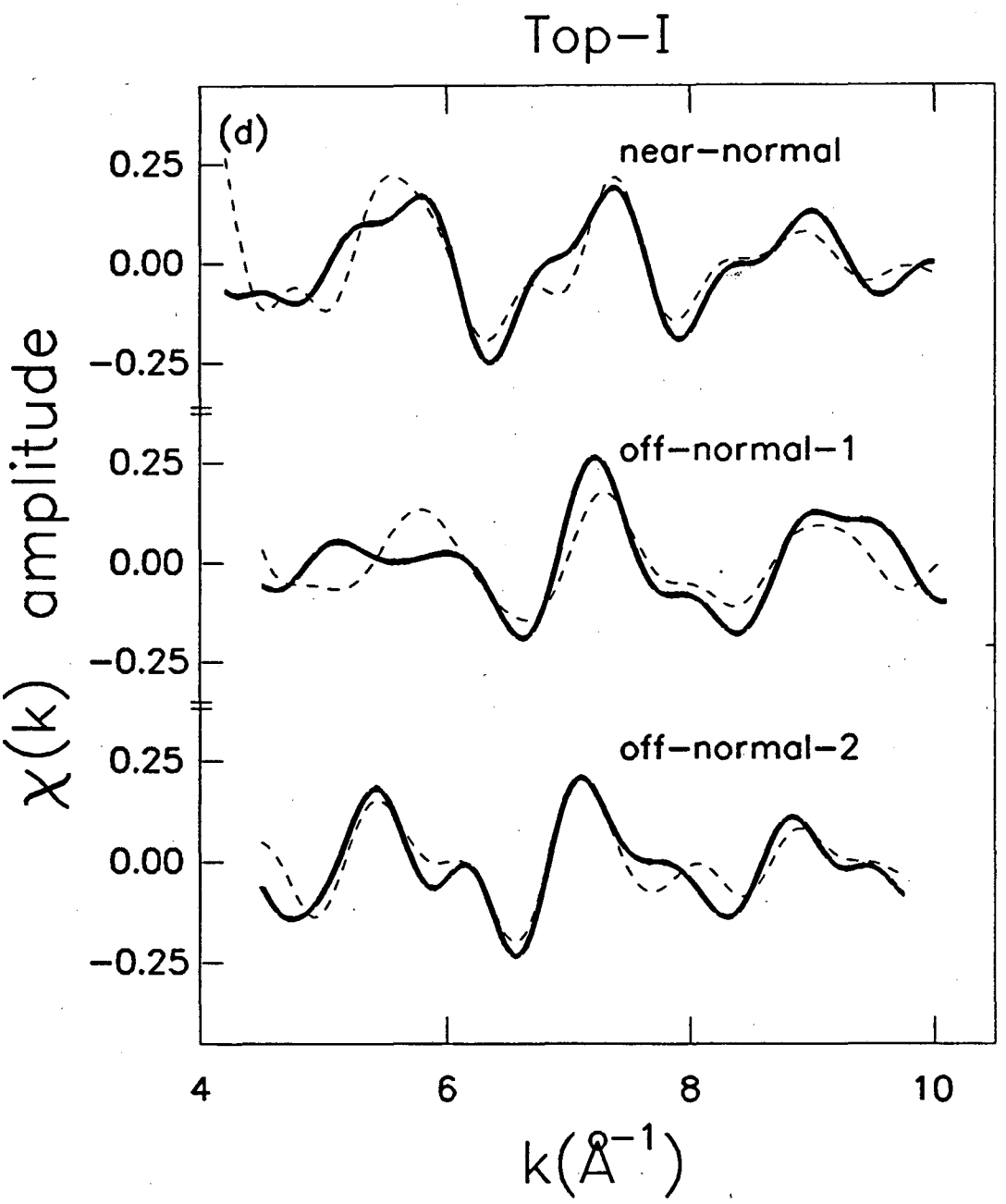
Top-I
(d)
near-normal
off-normal-1
off-normal-2
0.25
0.00
-0.25
0.25
0.00
-0.25
0.25
0.00
-0.25
χ(k) amplitude
4
6
8
10
k(Å^{-1})

FIGURE 7(d)

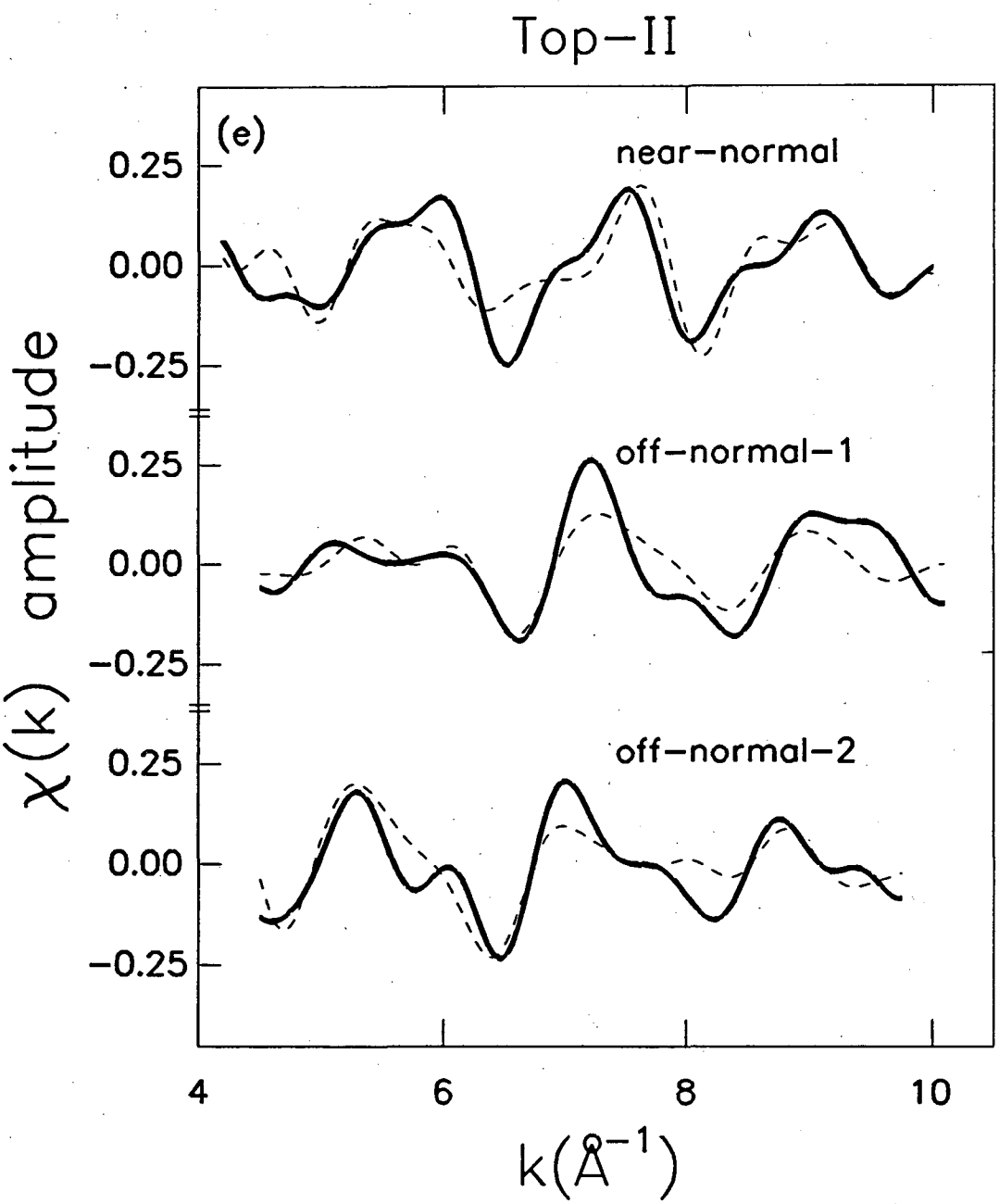
Top–II
(e)
near–normal
off–normal–1
off–normal–2
0.25
0.00
−0.25
χ(k) amplitude
4
6
8
10
k(Å^{-1})

FIGURE 7(e)

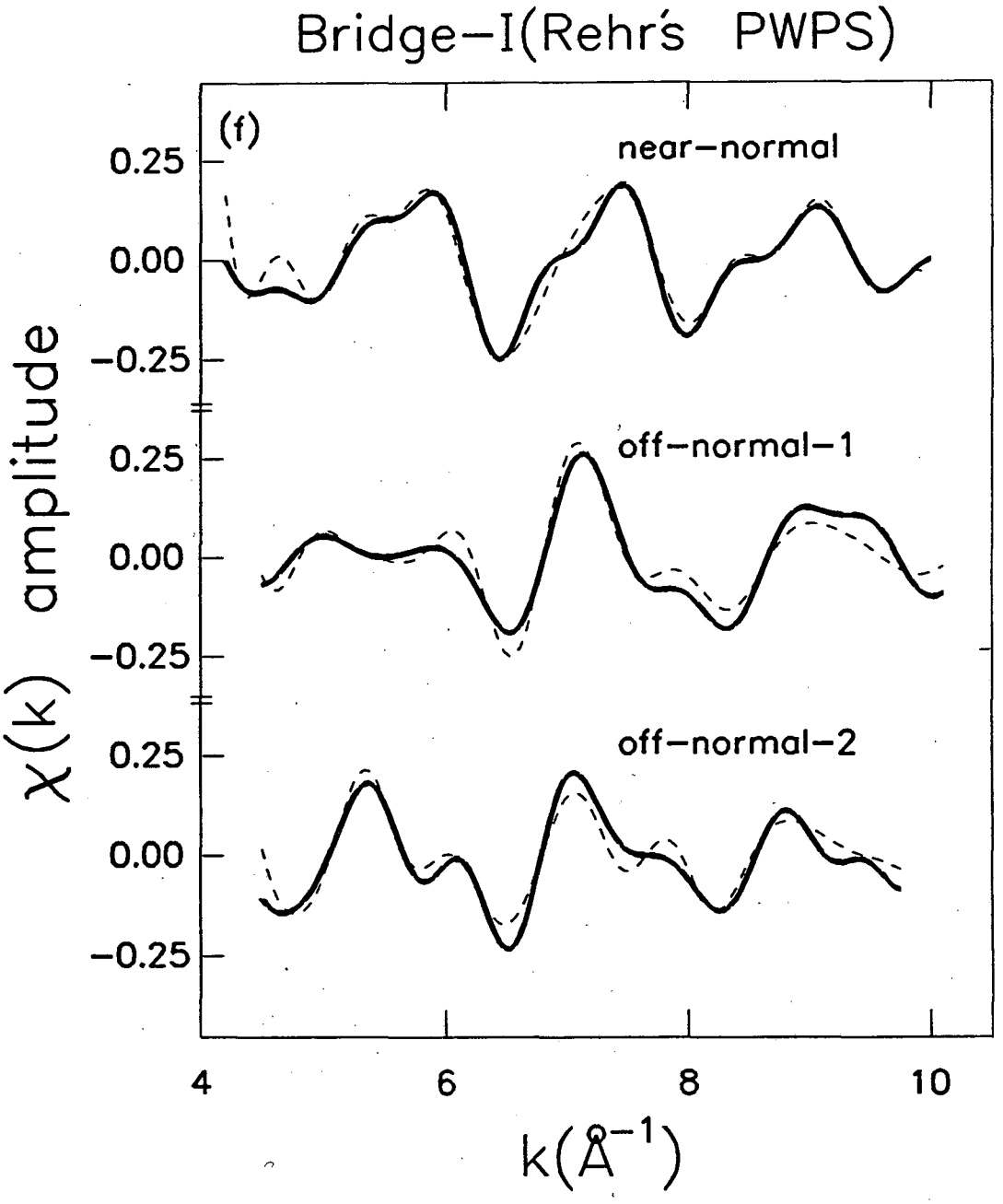
Bridge–I(Rehr's PWPS)
(f)
near–normal
off–normal–1
off–normal–2
0.25
0.00
–0.25
0.25
0.00
–0.25
0.25
0.00
–0.25
χ(k) amplitude
4
6
8
10
k(Å^{-1})

FIGURE 7(f)

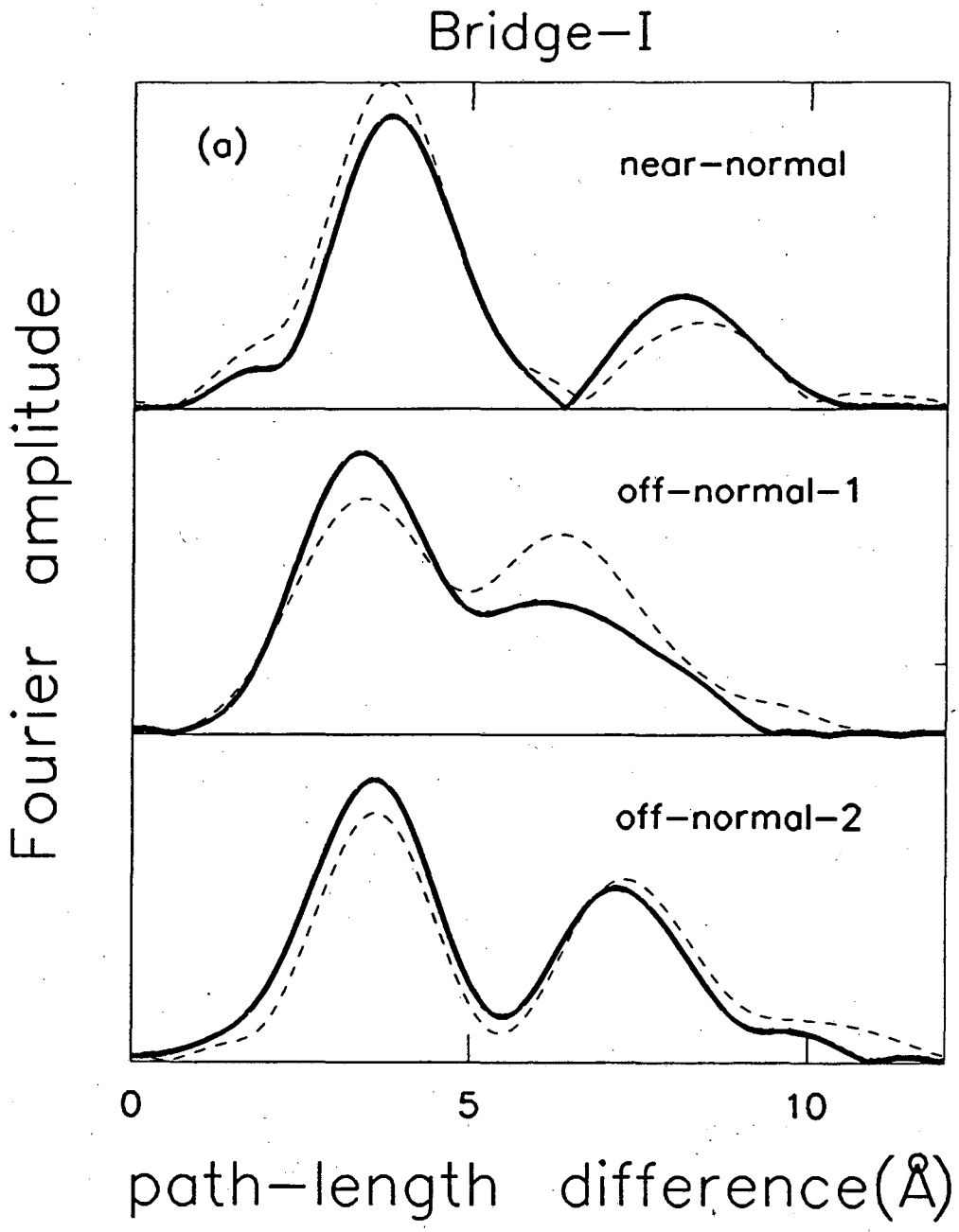
Bridge–I
(a)
near–normal
off–normal–1
off–normal–2
Fourier amplitude
0
5
10
path–length difference(Å)

FIGURE 8(a)

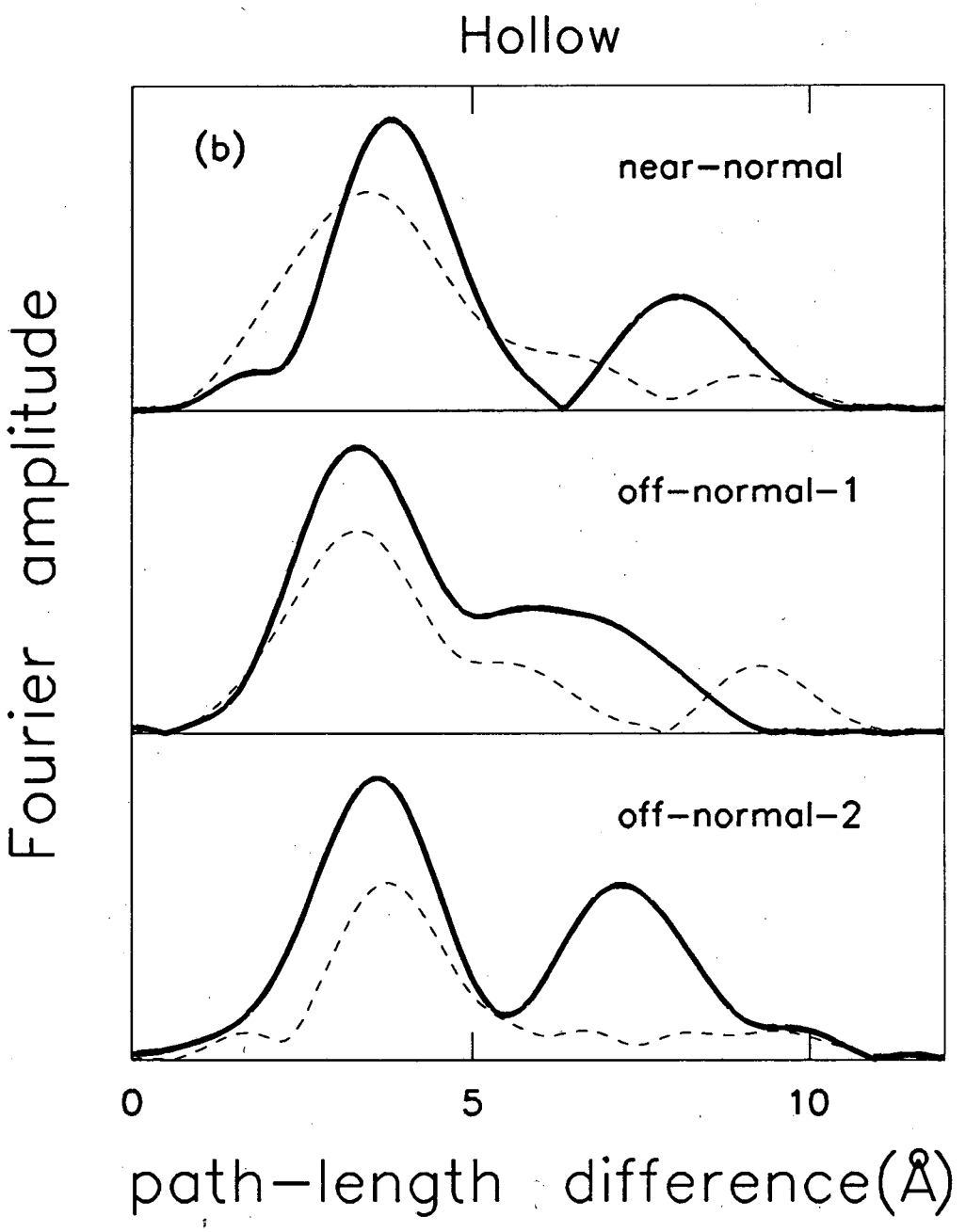
Hollow
(b)
near–normal
off–normal–1
off–normal–2
Fourier amplitude
0
5
10
path–length difference(Å)

FIGURE 8(b)

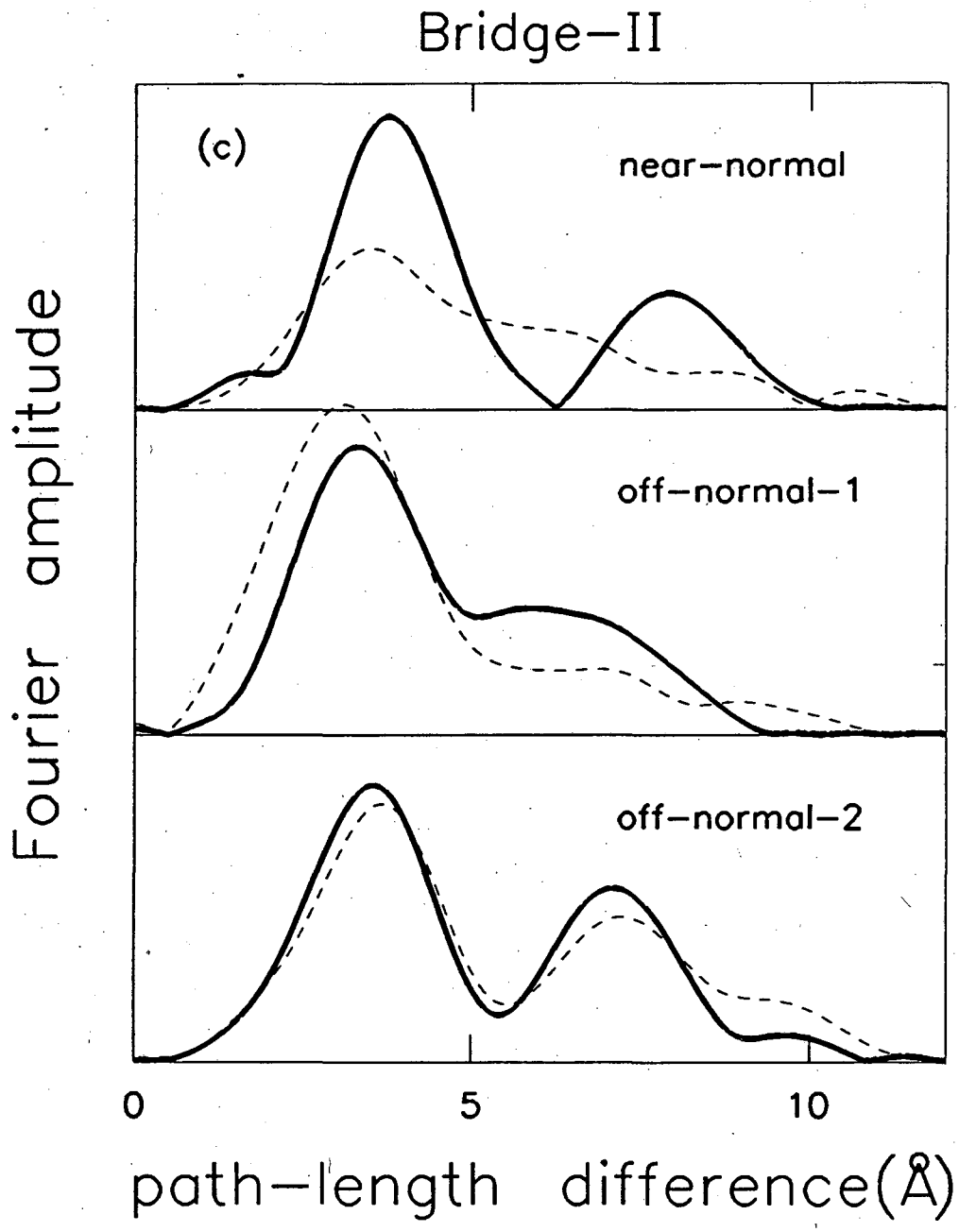
Bridge–II
(c)
near–normal
off–normal–1
off–normal–2
Fourier amplitude
0
5
10
path–length difference(Å)

FIGURE 8(c)

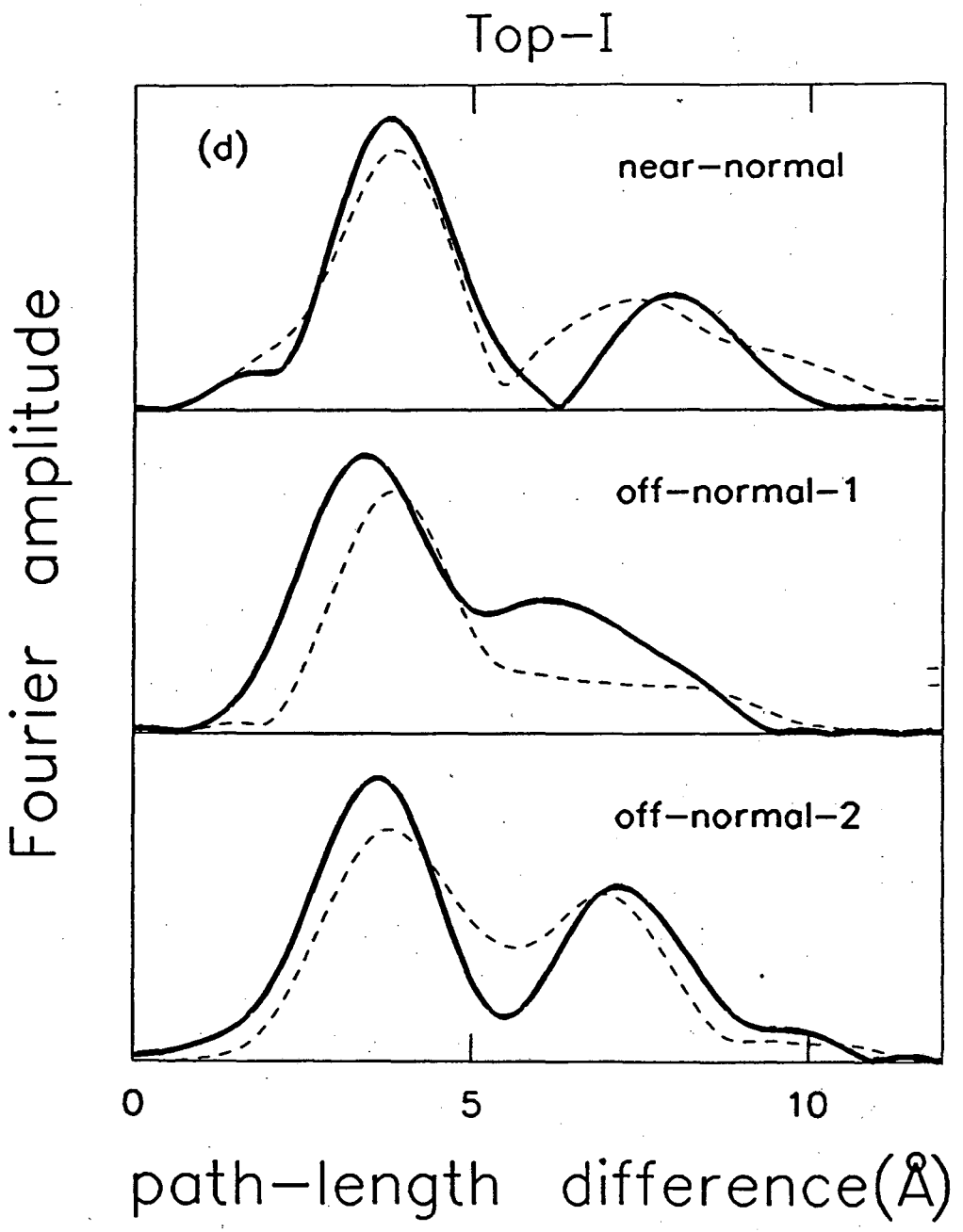
Top-I
(d)
near-normal
off-normal-1
off-normal-2
Fourier amplitude
0
5
10
path-length difference(Å)

FIGURE 8(d)

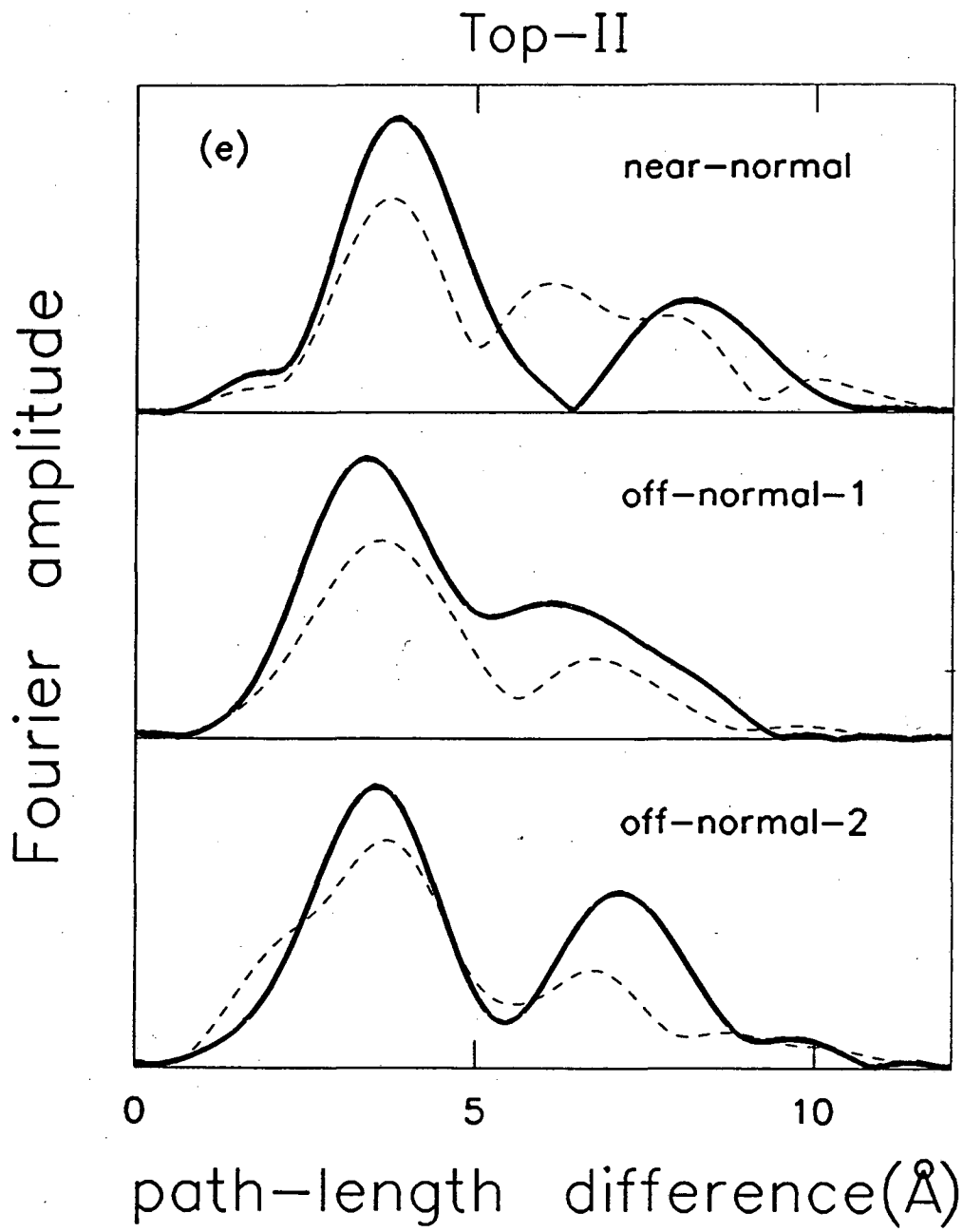
Top–II
(e)
near–normal
off–normal–1
off–normal–2
Fourier amplitude
0
5
10
path–length difference(Å)

FIGURE 8(e)

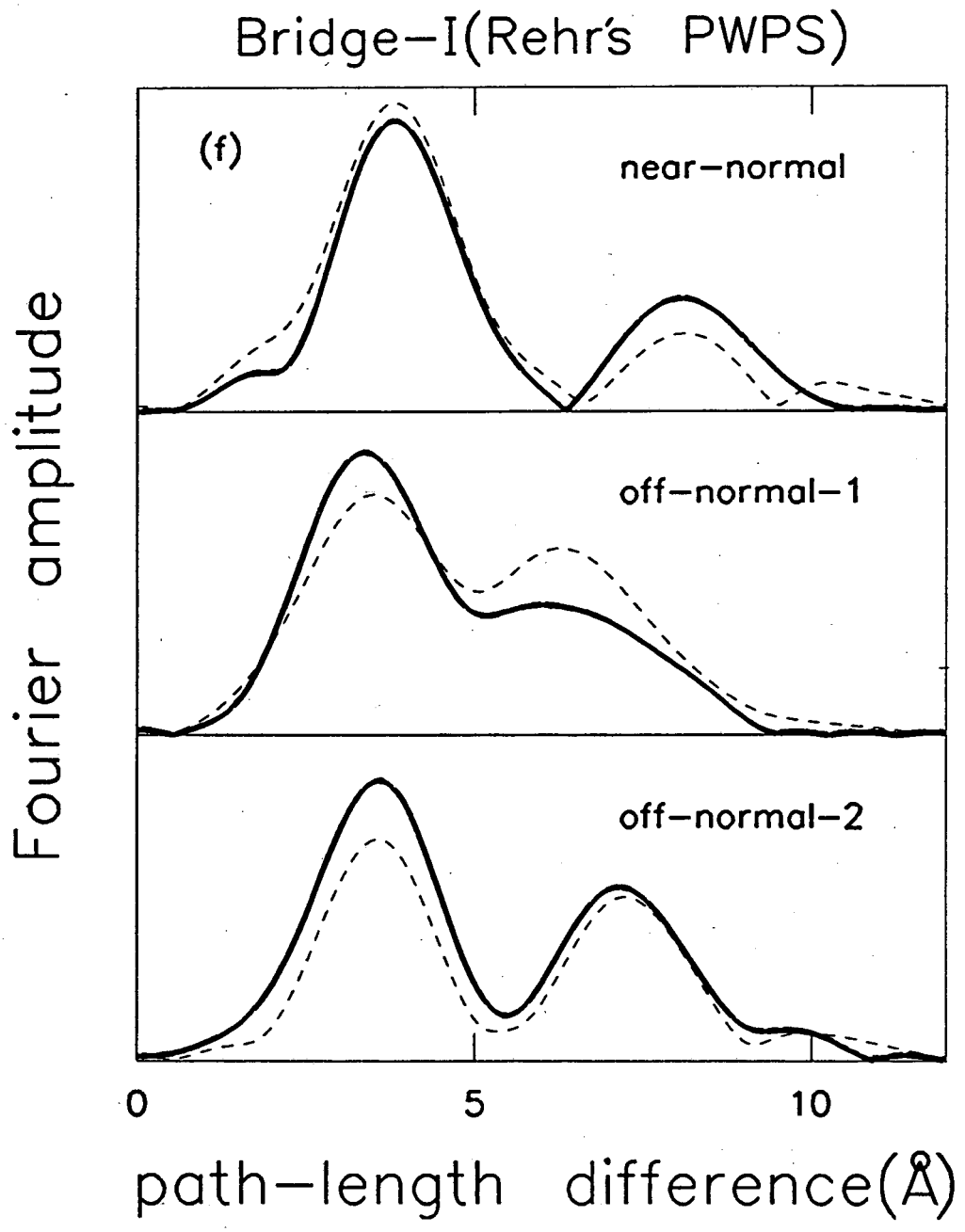
Bridge-I(Rehr's PWPS)
(f)
near-normal
off-normal-1
off-normal-2
Fourier amplitude
0
5
10
path-length difference(Å)

FIGURE 8(f)

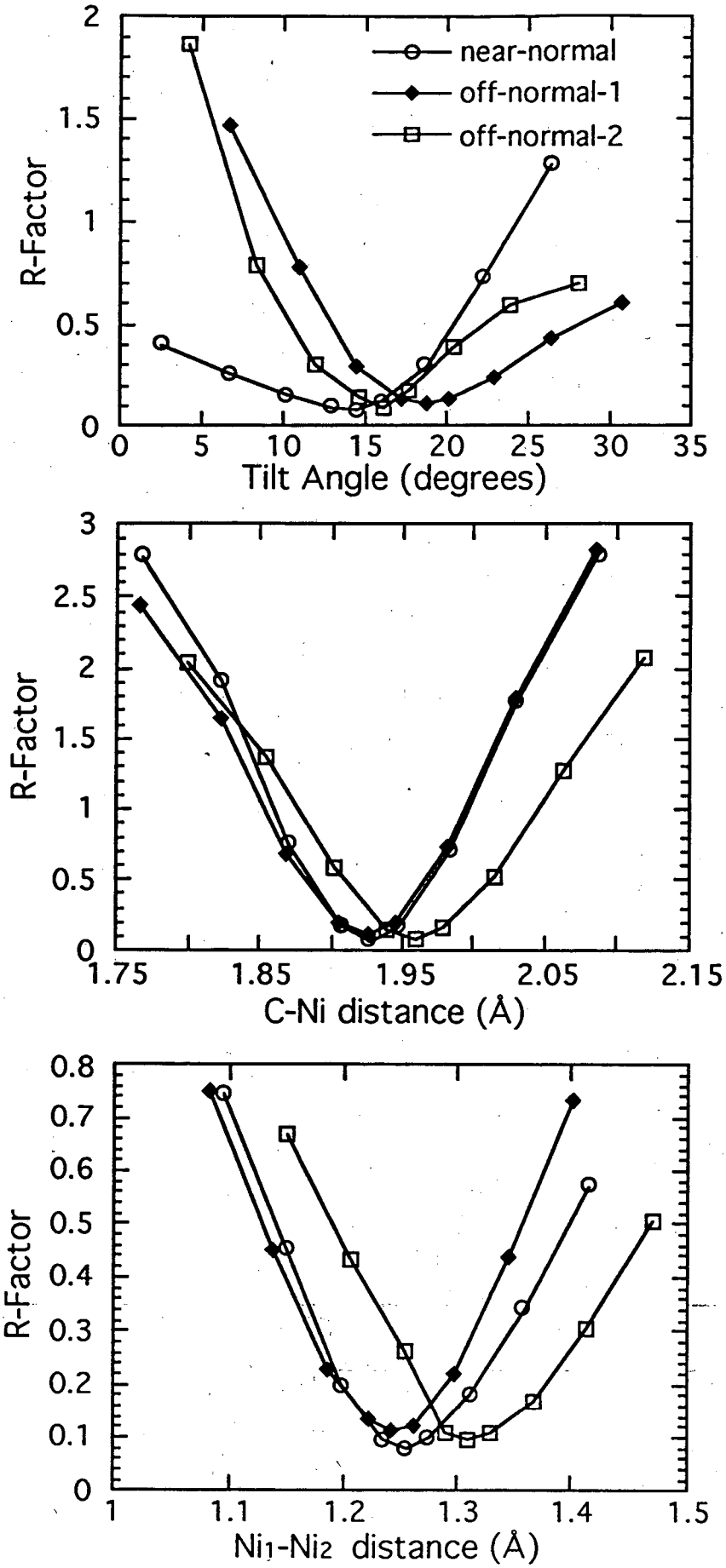
near-normal
off-normal-1
off-normal-2
R-Factor
Tilt Angle (degrees)
C-Ni distance (Å)
Ni1-Ni2 distance (Å)

FIGURE 9

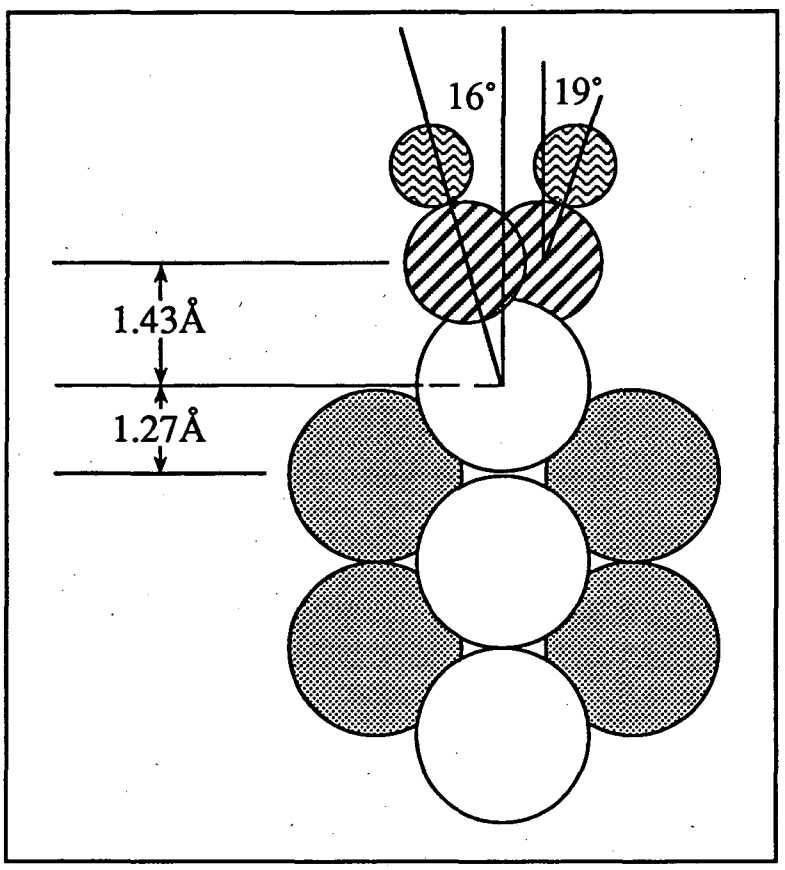

FIGURE 10

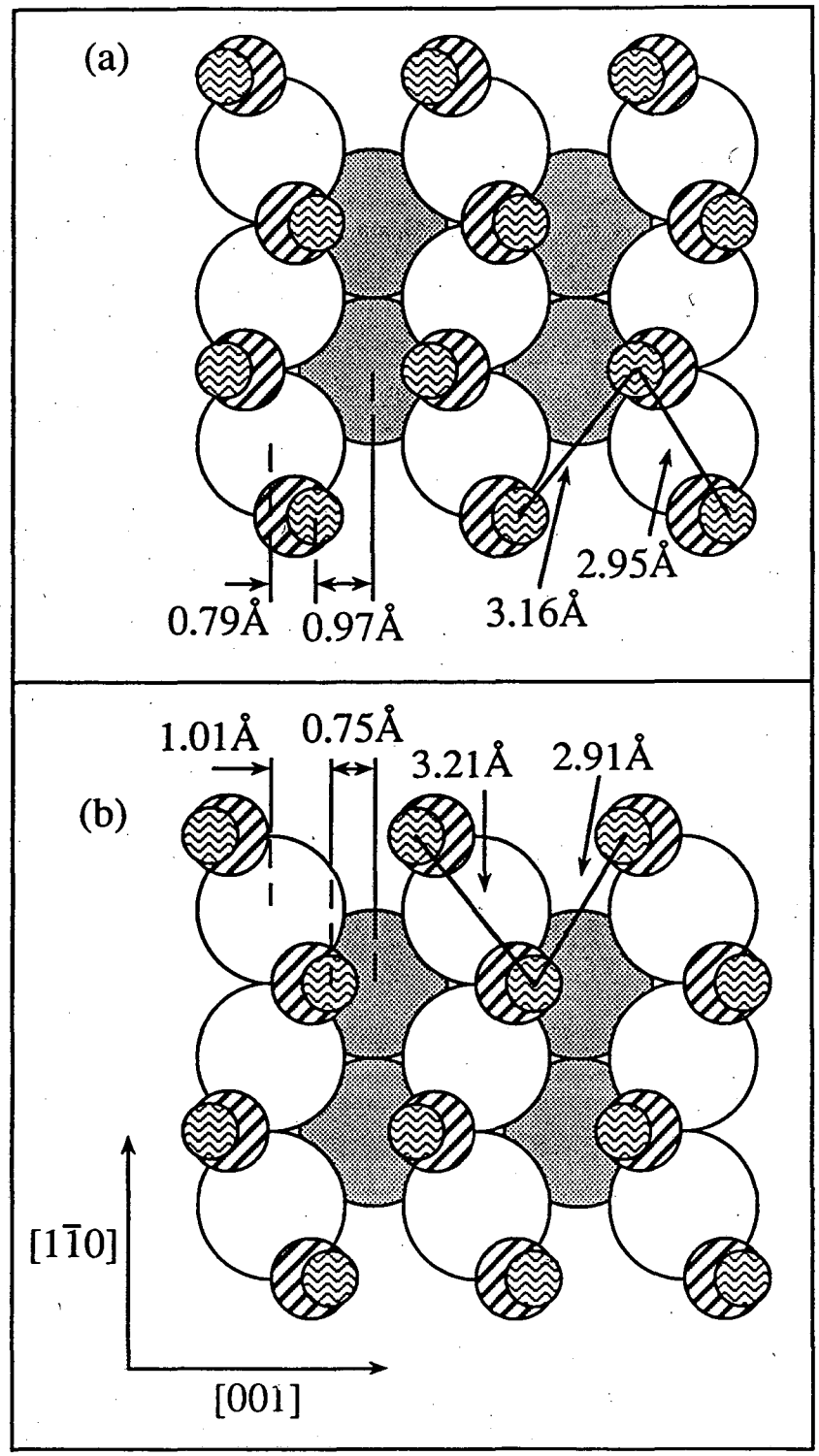

FIGURE 11

LAWRENCE BERKELEY LABORATORY
UNIVERSITY OF CALIFORNIA
TECHNICAL INFORMATION DEPARTMENT
BERKELEY, CALIFORNIA 94720